GaussainObject: Just Taking Four Images to Get A High-Quality 3D Object with Gaussian Splatting

CHEN YANG*, Shanghai Jiao Tong University, China
SIKUANG LI*, Shanghai Jiao Tong University, China
JIEMIN FANG†, Huawei, China
RUOFAN LIANG, University of Toronto, Canada
LINGXI XIE, Huawei, China
XIAOPENG ZHANG, Huawei, China
WEI SHEN‡, Shanghai Jiao Tong University, China
QI TIAN, Huawei, China

(a) 4 Input Views (b) Ground Truth (c) DietNeRF (d) FreeNeRF (e) 3DGS (f) Ours

Fig. 1. We introduce GaussianObject, a framework capable of reconstructing high-quality 3D objects from only 4 images with Gaussian splatting. GaussianObject demonstrates superior performance over previous SOTA methods on challenging objects.

Reconstructing and rendering 3D objects from highly sparse views is of critical importance for promoting applications of 3D vision techniques and improving user experience. However, images from sparse views only contain very limited 3D information, leading to two significant challenges: 1) Difficulty in building multi-view consistency as images for matching are too few; 2) Partially omitted or highly compressed object information as view coverage is insufficient. To tackle these challenges, we propose GaussianObject, a framework to represent and render the 3D object with Gaussian splatting, that achieves high rendering quality with only 4 input images. We first introduce techniques of visual hull and floater elimination which explicitly inject structure priors into the initial optimization process for helping build multi-view consistency, yielding a coarse 3D Gaussian representation. Then we construct a Gaussian repair model based on diffusion models to supplement the omitted object information, where Gaussians are further refined. We design a self-generating strategy to obtain image pairs for training the repair model. Our GaussianObject is evaluated on several challenging datasets, including MipNeRF360, OmniObject3D, and OpenIllumination, achieving strong reconstruction results from only 4 views and significantly outperforming previous state-of-the-art methods. Please visit our project page at https://gaussianobject.github.io/.

1 INTRODUCTION

Reconstructing and rendering 3D objects from 2D images has been a long-standing and important topic, which plays critical roles in a vast range of real-life applications. One key factor that impedes users, especially ones without expert knowledge, from widely using these techniques is that usually dozens of multi-view images need to be captured, which is cumbersome and sometimes impractical. Efficiently reconstructing high-quality 3D objects from highly sparse captured images is of great value for expediting downstream applications such as 3D asset creation for game/movie production and AR/VR products.

*Equal contribution.
†Project lead.
‡Corresponding author.

Authors' addresses: Chen Yang, ycyangchen@sjtu.edu.cn, Shanghai Jiao Tong University, Shanghai, China; Sikuang Li, whlisikuang@outlook.com, Shanghai Jiao Tong University, Shanghai, China; Jiemin Fang, jaminfong@gmail.com, Huawei, Shanghai, China; Ruofan Liang, ruofan@cs.toronto.edu, University of Toronto, Toronto, Canada; Lingxi Xie, 198808xc@gmail.com, Huawei, Shanghai, China; Xiaopeng Zhang, zxphistory@gmail.com, Huawei, Shanghai, China; Wei Shen, wei.shen@sjtu.edu.cn, Shanghai Jiao Tong University, Shanghai, China; Qi Tian, tian.qi1@huawei.com, Huawei, Shanghai, China.

In recent years, a series of methods [18, 36, 49, 55, 60, 72, 79, 81] have been proposed to reduce reliance on dense captures. However, it is still challenging to produce high-quality 3D objects when the views become **extremely sparse**, *e.g.* only 4 images in a 360° range, as shown in Fig. 1. We delve into the task of sparse-view reconstruction and discover two main challenges behind it. The first one lies in the difficulty of building multi-view consistency from highly sparse input. The 3D representation is easy to overfit the input images and degrades into fragmented pixel patches of training views without reasonable structures. The other challenge is that with sparse captures in a 360° range, some content of the object can be inevitably omitted or severely compressed when observed from extreme views[1]. The omitted or compressed information is impossible or hard to be reconstructed in 3D only from the input images.

To tackle the aforementioned challenges, we introduce GaussianObject, a novel framework designed to reconstruct high-quality 3D objects from as few as 4 input images. We choose 3D Gaussian splitting (3DGS) [22] as the basic representation as it is fast and, more importantly, explicit enough. Benefiting from its point-like structure, we design several techniques for introducing object structure priors, *e.g.* the basic/rough geometry of the object, to help build multi-view consistency, including visual hull [26] to locate Gaussians within the object outline and floater elimination to remove outliers. To erase artifacts caused by omitted or highly compressed object information, we propose a Gaussian repair model driven by 2D large diffusion models [44] which translates corrupted rendered images into high-fidelity ones. As normal diffusion models lack the ability to repair corrupted images, we design self-generating strategies to construct image pairs to tune the diffusion models, including rendering images from leave-one-out training models and adding 3D noises to Gaussian attributes. Images generated from the repair model can be used for refining the 3D Gaussians optimized with structure priors, where the rendering quality can be further improved.

Our contributions are summarized as follows:

- We propose to optimize 3D Gaussians from highly sparse views with explicit structure priors, where several techniques are designed, including the visual hull for initialization and floater elimination for training.
- A Gaussian repair model based on diffusion models is proposed to remove artifacts caused by omitted or highly compressed object information, where the rendering quality can be further improved.
- The overall framework GaussianObject shows strong performance on several challenging real-world datasets, consistently outperforming previous state-of-the-art methods for both qualitative and quantitative evaluation.

[1]When the view is orthogonal to the surface of the object, the observed information attached to the surface can be largely reserved; On the contrary, the information will be severely compressed.

2 RELATED WORKS

2.1 Differentiable Point-based Rendering

Recent studies, such as DSS [74] and SynSin [64], have introduced differentiable point-based rendering methods to effectively utilize information from point clouds. These methods enhance point clouds with additional features and employ neural networks to convert these features into images. Point-NeRF [70] accelerates the neural radiance field (NeRF) [35] by rendering discrete neural points, yet it still requires a few seconds to render an image. Point-Radiance [77] employs spherical harmonics to represent the color of points and utilizes a splatting strategy for real-time rendering. Built upon these advancements, 3DGS [22] integrates 3D Gaussians, achieving high-quality reconstruction of real-world scenes at real-time speeds. However, point-based methods heavily depend on precise and dense initial point configurations, a significant hurdle in sparse 360° reconstruction. To address this challenge, our approach integrates object structure priors, providing a robust solution for sparse setups.

2.2 Neural Rendering for Sparse View Reconstruction

Vanilla NeRF struggles in sparse settings. Techniques like Deng et al. [9], Roessle et al. [43], Somraj et al. [52], Somraj and Soundararajan [53] use SfM-derived [46] visibility or depth mainly focus on closely aligned views. [69] uses ground truth depth maps, which are costly to obtain in real-world images. Some methods [55, 60] estimate depths with monocular depth estimation models[40, 42] or sensors, but these are often too coarse. [18] uses a vision-language model[39] for unseen view rendering, but the semantic consistency is too high-level to guide low-level reconstruction. [49] combines a deep image prior with factorized NeRF, effectively capturing overall appearance but missing fine details in input views. Priors based on information theory[23], continuity[36], symmetry[47], and frequency regularization[72] are effective for specific scenarios, limiting their further applications. Besides, there are some methods [16, 19, 20, 62, 71, 82] that employ Visual Transformer (ViT)[11] to reduce the requirements for constructing NeRFs.

The recent progress in text-to-image diffusion models like the Latent Diffusion Model (LDM) [44] has spurred notable advancements in 3D applications. Dreamfusion [38] proposes Score Distillation Sampling (SDS) for distilling NeRFs with 2D priors from a pre-trained diffusion model for 3D object generation from text prompts. It has been further refined for text-to-3D [6, 27, 34, 50, 59, 61, 63, 73] and 3D/4D editing [14, 48] by various studies, demonstrating the versatility of 2D diffusion models in 3D contexts. Chan et al. [4], Liu et al. [29], Zhu and Zhuang [80] have adapted these methods for 3D generation and view synthesis from single images, although these often have strict input requirements and can produce overly saturated images. In sparse reconstruction, approaches like DiffusioNeRF [67], SparseFusion [79], Deceptive-NeRF [30] and ReconFusion [65] integrate diffusion models with NeRFs, which require pertaining on substantial 3D data.

While 3D Gaussian splatting (3DGS) shows strong power in novel view synthesis, it struggles with sparse 360° views similar to NeRF. Inspired by few-shot NeRFs, methods [7, 68, 81] have been developed for sparse 360° reconstruction. However, these methods still severely

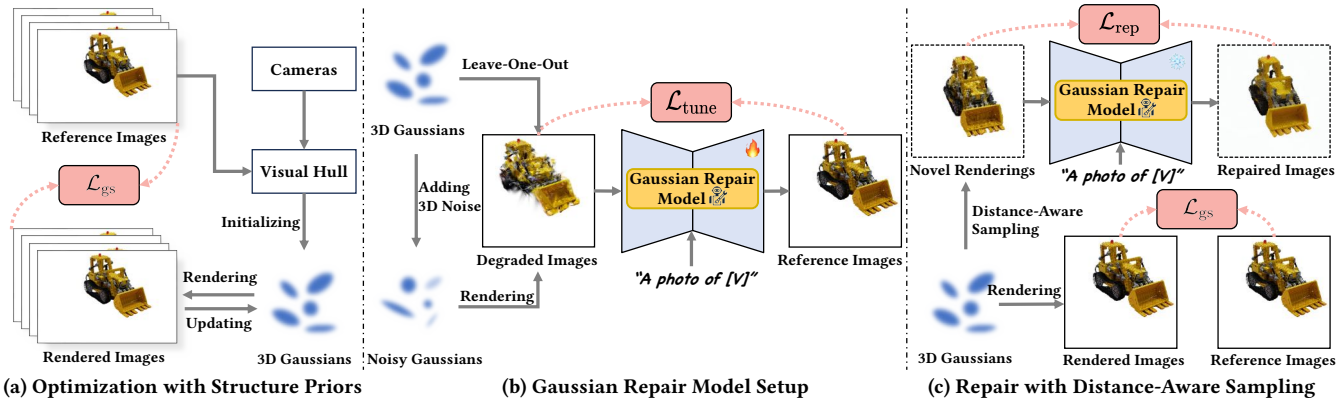

(a) Optimization with Structure Priors **(b) Gaussian Repair Model Setup** **(c) Repair with Distance-Aware Sampling**

Fig. 2. (a) We initialize 3D Gaussians by constructing a visual hull with camera parameters and masked images, optimizing them with the $\mathcal{L}_{gs}$ and refining through floater elimination. (b) We use a novel 'leave-one-out' strategy and add 3D noise to Gaussians to generate corrupted Gaussian renderings. These renderings, paired with their corresponding reference images, facilitate the training of the Gaussian repair model employing $\mathcal{L}_{tune}$. (c) Once trained, the Gaussian repair model is frozen and used to correct views that need to be rectified. These views are identified through distance-aware sampling. The repaired images and reference images are used to further optimize 3D Gaussians with $\mathcal{L}_{rep}$ and $\mathcal{L}_{gs}$.

rely on the SfM points. Our GaussianObject proposes structure-prior-aided Gaussian initialization to tackle this issue, drastically reducing the required input views to only 4, a significant improvement compared with over 20 views required by FSGS [81].

3 METHOD

The subsequent sections detail the methodology: Sec. 3.1 reviews foundational techniques; Sec. 3.2 introduces our overall framework; Sec. 3.3 describes how we take full advantage of the structure priors for initial optimization; Sec. 3.4 details the setup of our Gaussian repair model, and Sec. 3.5 illustrates the repair of 3D Gaussians using this model.

3.1 Preliminary

3D Gaussian Splatting. 3D Gaussian Splatting [22] represents a 3D scene with 3D Gaussians. Each 3D Gaussian is composed of the center location μ, rotation quaternion q, scaling vector s, opacity σ, and spherical harmonic (SH) coefficients sh. Thus, a scene is parameterized as a set of Gaussians $\mathcal{G} = \{G_i : \mu_i, q_i, s_i, \sigma_i, sh_i\}_{i=1}^{P}$. 3DGS employs the neural point-based α-blending technique to render the color $C(u)$ of a pixel u. Considering the view direction v_i, the pixel color is computed as:

$$C(u) = \sum_{i \in N} \mathrm{SH}(sh_i, v_i)\alpha_i \prod_{j=1}^{i-1}(1-\alpha_j), \quad \alpha_i = \sigma_i G_i(p). \tag{1}$$

Diffusion Models and ControlNet. Diffusion models [10, 51, 56] are a category of generative models capable of sampling realistic images from data distribution $q(X_0)$, starting with Gaussian noise ϵ. This is achieved using various sampling schedulers [12, 15, 21, 32, 54, 57]. The main process involves reversing a discrete-time stochastic process $\{X_t\}_{t=0}^{T}$, represented as:

$$X_t = \sqrt{\bar{\alpha}_t}X_0 + \sqrt{1-\bar{\alpha}_t}\epsilon, \text{ where } \epsilon \sim \mathcal{N}(0, I), \tag{2}$$

where $t \in [0, T]$ is the noise level and $\bar{\alpha}_{1:T} \in (0, 1]^T$ is a decreasing sequence. In the reversed process, a diffusion model $p_\theta(X_{t-1}|X_t)$ is trained to approximate $q(X_{t-1}|X_t)$. Substituting X_0 with its latent code Z_0 from a Variational Autoencoder (VAE) [24] leads to the development of Latent Diffusion Models (LDM) [44]. ControlNet [75] further enhances the generative process with additional image conditioning by integrating a network structure similar to the diffusion model, which slightly changes the loss function to:

$$\mathcal{L}_{Cond} = \mathbb{E}_{Z_0,t,\epsilon}[\|\epsilon_\theta(\sqrt{\bar{\alpha}_t}Z_0 + \sqrt{1-\bar{\alpha}_t}\epsilon, t, c^{\text{tex}}, c^{\text{img}}) - \epsilon\|_2^2], \tag{3}$$

where c^{tex} and c^{img} denote the text and image conditioning respectively.

3.2 Overall Framework

Given a sparse collection of N reference images $X^{\text{ref}} = \{x_i\}_{i=1}^{N}$, captured within a 360° range and encompassing one object, along with the corresponding camera parameters $\Pi^{\text{ref}} = \{\pi_i\}_{i=1}^{N}$ and masks $M^{\text{ref}} = \{m_i\}_{i=1}^{N}$ of the object, our target is to obtain a 3D representation $\mathcal{G}$, which can achieve photo-realistic rendering from any viewpoint $x = \mathcal{G}(\pi|\{x_i, \pi_i, m_i\}_{i=1}^{N})$. To achieve this, we employ the 3DGS model for its simplicity for structure priors embedding and fast rendering capabilities. The process begins with initializing 3D Gaussians using a visual hull [26], followed by optimization with floater elimination, enhancing the structure of Gaussians. Then we design self-generating strategies to supply sufficient image pairs for constructing a Gaussian repair model, which is used to rectify incomplete object information. Our overall framework is shown in Fig. 2.

3.3 Initial Optimization with Structure Priors

Sparse views, especially for only 4 images, provide very limited 3D information for reconstruction. In this case, SfM points, which are the key for 3DGS initialization, are often absent. Besides, insufficient multi-view consistency leads to ambiguity among shape

and appearance, resulting in many floaters during reconstruction. We propose two techniques to initially optimize the 3D Gaussian representation, which take full advantage of structure priors from the limited views and result in a satisfactory outline of the object.

Initialization with Visual Hull To better leverage object structure information from limited reference images, we utilize the view frustums and object masks to create a visual hull that serves as a geometric scaffold for initializing our 3D Gaussians. Compared with few SfM points that contain little valid information, the visual hull provides more structure priors that help build multi-view consistency by excluding unreasonable Gaussian distributions. The cost of the visual hull is just several masks of sparse 360° images, which can be easily acquired via segmentation model [25]. Specifically, points are randomly initialized within the visual hull using rejection sampling: we project uniformly sampled random 3D points onto image planes and retain those within the intersection of all image-space masks. Point colors are averaged from bilinearly interpolated pixel colors across reference image projections. Then we transform these 3D points into 3D Gaussians. For each point, we assign its position as μ and convert its color into sh. The mean distance between adjacent points is used to form the scale s, while the rotation q is set to a unit quaternion as default. The opacity σ is initialized to a constant value. This initialization strategy relies on the initial masks. Despite potential inaccuracies in these masks or unrepresented concavities by the visual hull, we have observed that subsequent optimization processes reliably yield high-quality reconstructions.

Floater Elimination While the visual hull builds a coarse estimation of the object geometry, it often contains regions that do not belong to the object due to the inadequate coverage of reference images. These regions usually appear to be floaters which damage the quality of novel view synthesis. These floaters are problematic as the optimization process struggles to adjust them due to insufficient observational data regarding their position and appearance.

To mitigate this issue, we propose to utilize the statistical distribution of distances among the 3D Gaussians to distinguish the primary object and the floaters. This is implemented by the K-Nearest Neighbors (KNN) algorithm, which calculates the average distance to the nearest $\sqrt{P}$ Gaussians for each element in $\mathcal{G}_c$. We then establish a normative range by computing the mean and standard deviation of these distances. Based on this statistical analysis, we exclude any Gaussian whose mean neighbor distance exceeds the adaptive threshold τ. This thresholding process is repeated periodically throughout optimization, where τ is linearly decreased to 0 to progressively refine the scene representation.

Initial Optimization The optimization of $\mathcal{G}_c$ incorporates color, mask, and monocular depth losses. The color loss combines L1 and D-SSIM losses:

$$\mathcal{L}_1 = \|x - x^{\text{ref}}\|_1, \quad \mathcal{L}_{\text{D-SSIM}} = 1 - \text{SSIM}(x, x^{\text{ref}}), \tag{4}$$

where x is the rendering and x^{ref} is the corresponding reference image. A binary cross entropy (BCE) loss is applied as mask loss:

$$\mathcal{L}_{\text{m}} = -(m^{\text{ref}} \log m + (1 - m^{\text{ref}}) \log(1 - m)), \tag{5}$$

where m denotes the object mask. A shift and scale invariant depth loss is utilized to guide geometry:

$$\mathcal{L}_{\text{d}} = \|D^* - D^*_{\text{pred}}\|_1, \tag{6}$$

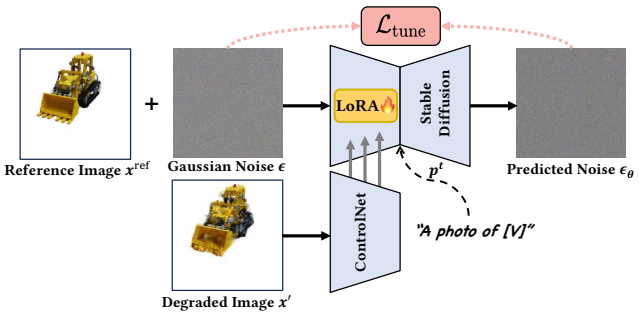

Fig. 3. Illustration of the optimization of our Gaussian repair model.

where D^* and D^*_{pred} are per-frame rendered depths and monocularly estimated depths [2] respectively. The depth values are computed following a normalization strategy [41]:

$$D^* = \frac{D - \text{median}(D)}{\frac{1}{M}\sum_{i=1}^{M} |D - \text{median}(D)|}, \tag{7}$$

where M denotes the number of valid pixels. The overall loss combines these components as

$$\mathcal{L}_{gs} = (1 - \lambda_{\text{SSIM}})\mathcal{L}_1 + \lambda_{\text{SSIM}}\mathcal{L}_{\text{D-SSIM}} + \lambda_{\text{m}}\mathcal{L}_{\text{m}} + \lambda_{\text{d}}\mathcal{L}_{\text{d}}, \tag{8}$$

where λ_{SSIM}, λ_{m}, and λ_{d} control the magnitude of each term. Thanks to the efficient initialization, our training speed is remarkably fast. It only takes 1 minute to train a coarse Gaussian representation $\mathcal{G}_c$ at a resolution of 779×520.

3.4 Gaussian Repair Model Setup

The integration of visual hull initialization with a floater elimination strategy remarkably improves the performance of 3DGS for novel view synthesis in sparse 360° contexts. While the fidelity of our reconstruction is generally passable, $\mathcal{G}_c$ still suffers in regions that are poorly observed, regions with occlusion, or even unobserved regions. These challenges loom over the completeness of the reconstruction like the sword of Damocles.

To mitigate these issues, we introduce a Gaussian repair model $\mathcal{R}$ designed to correct the aberrant distribution of $\mathcal{G}_c$. Our $\mathcal{R}$ is powered by 2D diffusion models, which takes corrupted rendered images $x'(\mathcal{G}_c, \pi^{\text{nov}})$ as input and outputs photo-realistic and high-fidelity images $\hat{x}$. This image repair capability can be used to refine the 3D Gaussians, leading to learn better structure and appearance details.

Sufficient data pairs are essential for training $\mathcal{R}$ but are rare in existing datasets. To this end, we adopt two main strategies for generating adequate image pairs, *i.e.*, **leave-one-out training** and **adding 3D noises**. For leave-one-out training, we build N subsets from the N input images, each containing $N - 1$ reference images and 1 left-out image x^{out}. Then we train N 3DGS models with reference images of these subsets, termed as $\{\mathcal{G}_c^i\}_{i=0}^{N-1}$. After specific iterations, we use the left-out image x^{out} to continue training each Gaussian model $\{\mathcal{G}_c^i\}_{i=0}^{N-1}$ into $\{\hat{\mathcal{G}}_c^i\}_{i=0}^{N-1}$. Throughout this process, the rendered images from the left-out view at different iterations are stored to form the image pairs along with left-out image x^{out} for training the repair model. Note that training these left-out models

cost little, with less than N minutes in total. The other strategy is to add 3D noises ϵ_s onto the attributes of Gaussians. The ϵ_s are derived from the mean μ_Δ and variance σ_Δ of attribute differences between $\{\mathcal{G}_c^i\}_{i=0}^{N-1}$ and $\{\hat{\mathcal{G}}_c^i\}_{i=0}^{N-1}$. This allows us to render more degraded images $x'(\mathcal{G}_c(\epsilon_s), \pi^{\text{ref}})$ at all reference views from the created noisy Gaussians, resulting in extensive image pairs (X', X^{ref}).

We inject LoRA weights and fine-tune a pre-trained ControlNet [76] using the generated image pairs to serve as our Gaussian repair model. The training procedure is shown in Fig. 3. The loss function, based on Eq. 3, is defined as:

$$\mathcal{L}_{\text{tune}} = \mathbb{E}_{x^{\text{ref}},t,\epsilon,x'}\left[\|(\epsilon_\theta(x_t^{\text{ref}}, t, x', c^{\text{tex}}) - \epsilon)\|_2^2\right], \tag{9}$$

where c^{tex} denotes an object-specific language prompt, defined as "a photo of [V]," as per Dreambooth [45]. Specifically, we inject LoRA layers into the text encoder, image condition branch and U-Net for fine-tuning. Please refer to the Appendix for details.

3.5 Gaussian Repair with Distance-Aware Sampling

After training $\mathcal{R}$, we distill its target object priors into $\mathcal{G}_c$ to refine its rendering quality. The object information near the reference views is abundant. This observation motivates designing distance as a criterion in identifying views that need to be rectified, leading to distance-aware sampling.

Specifically, we establish an elliptical path aligned with the training views and focus on a central point. Arcs near Π^{ref}, where we assume $\mathcal{G}_c$ renders high-quality images, form the reference path. The other arcs, yielding renderings need to be rectified, define the repair path, as depicted in Fig. 4. In each iteration, novel viewpoints, $\pi_j \in \Pi^{\text{nov}}$, are randomly sampled among the repair path. For each π_j, we render the corresponding image $x_j = x_j(\mathcal{G}_c, \pi_j)$, encode it to be $\mathcal{E}(x_j)$ by the latent diffusion encoder $\mathcal{E}$ and pass $\mathcal{E}(x_j)$ to the image conditioning branch of $\mathcal{R}$. Simultaneously, a cloned $\mathcal{E}(x_j)$ is disturbed into a noisy latent z_t:

$$\begin{aligned} z_t &= \sqrt{\bar{\alpha}_t}\mathcal{E}(x_j) + \sqrt{1-\bar{\alpha}_t}\epsilon, \\ &\text{where } \epsilon \sim \mathcal{N}(0, I), t \in [0, T], \end{aligned} \tag{10}$$

which is similar to SDEdit [33]. We then generate a sample $\hat{x}_j$ from $\mathcal{R}$ by running DDIM sampling [54] over $k = \lfloor 50 \cdot \frac{t}{T} \rfloor$ steps and forwarding the diffusion decoder $\mathcal{D}$:

$$\hat{x}_j = \mathcal{D}(\text{DDIM}(z_t, \mathcal{E}(x_j))). \tag{11}$$

The distance from π_j to π^{ref} is used to weight the reliability of $\hat{x}_j$, guiding the optimization with a loss function:

$$\begin{aligned} \mathcal{L}_{\text{rep}} &= \mathbb{E}_{\pi_j,t}\left[w(t)\lambda(\pi_j)\left(\|x_j - \hat{x}_j\|_1 + \|x_j - \hat{x}_j\|_2 + L_p(x_j, \hat{x}_j)\right)\right], \\ &\text{where } \lambda(\pi_j) = \frac{2 \cdot \min_{i=1}^{N}(\|\pi_j - \pi_i\|_2)}{d_{\max}}. \end{aligned} \tag{12}$$

Here, L_p denotes the perceptual similarity metric LPIPS [78], $w(t)$ is a noise-level modulated weighting function, $\lambda(\pi_j)$ denotes a distance-based weighting function, and $d_{\max}$ is the maximal distance among neighboring reference viewpoints. To ensure coherence between 3D Gaussians and reference images, we continue training $\mathcal{G}_c$ with $\mathcal{L}_{\text{gs}}$ during the whole Gaussian repair procedure.

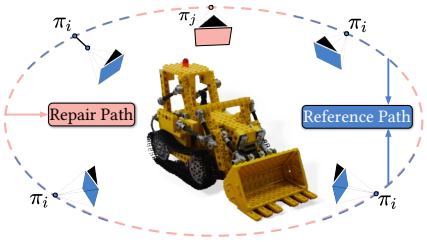

Fig. 4. Illustration of our distance-aware sampling. Blue and red indicate the reference and repair path, respectively.

4 EXPERIMENTS

4.1 Implementation Details

Our framework, illustrated in Fig. 2, is based on 3DGS [22] and threestudio [13]. The 3DGS model is trained for 10k iterations in the initial optimization, with periodic floater elimination every 500 iterations. We inherent densification and reset opacity from 3DGS, with every 100 and 1000 iterations. The monocular depth for $\mathcal{L}_{\text{d}}$ is predicted by ZoeDepth [2].

In the Gaussian repair model setup, the backbone is a ControlNet-Tile [76] model based on stable diffusion v1.5 [44], optimized using an AdamW optimizer [31] with β values of $(0.9, 0.999)$. LoRA [17] weights, injected into the text-encoder and transformer blocks using minLoRA [5], are trained for 1800 steps at a LoRA rank of 64 and a learning rate of 10^{-3}.

$\mathcal{G}_c$ is trained for another 4k iterations during distance-aware sampling. For the first 2800 iterations, optimization involves both a reference image and a repaired novel view image, with the weight of $\mathcal{L}_{\text{rep}}$ progressively decayed from 1.0 to 0.1. The final 1200-step training only involves reference views. The whole process of GaussianObject takes about 30 minutes on a GeForce RTX 3090 GPU for 4 input images at a 779×520 resolution.

4.2 Datasets

We evaluate our proposed method on three datasets suited for sparse-view 360° object reconstruction with varying input views, including Mip-NeRF360 [1], OmniObject3D [66], and OpenIllumination [28]. For datasets that do not provide object masks, we employ SA3D [3] to get the target object masks. More details about datasets can be referred to in the Appendix.

4.3 Evaluation

We evaluate the performance of GaussianObject against several reconstruction baselines, including the vanilla 3DGS [22] with random initialization and DVGO [58], and various few-view reconstruction models on the three datasets. Compared methods of RegNeRF [36], DietNeRF [18], SparseNeRF [60], and ZeroRF [49] utilize a variety of regularization techniques. Besides, FSGS [81] is also built upon Gaussian splatting with SfM-point initialization. Note that we supply extra SfM points to FSGS so that it can work with the highly sparse 360° setting. All models are trained using the publicly released implementation codes, with further implementation details available in the Appendix.

Fig. 5. Qualitative examples on the MipNeRF360 and OmniObject3D dataset with 4 input views. Many methods fail to reach a coherent 3D representation, resulting in floaters and disjoint pixel patches. Note that a pure white image indicates a total miss of the object by the corresponding method usually caused by an overfitting to the input images.

Table 1. Comparisons on MipNeRF360 and OmniObject3D datasets with varying input views. LPIPS* = LPIPS $\times 10^2$ throughout this paper.

	Method	4-view			6-view			9-view		
		LPIPS* ↓	**PSNR** ↑	**SSIM** ↑	**LPIPS*** ↓	**PSNR** ↑	**SSIM** ↑	**LPIPS*** ↓	**PSNR** ↑	**SSIM** ↑
MipNeRF360	DVGO [58]	24.43	14.39	0.7912	26.67	14.30	0.7676	25.66	14.74	0.7842
	3DGS [22]	10.80	20.31	0.8991	8.38	22.12	0.9134	6.42	24.29	0.9331
	DietNeRF [18]	11.17	18.90	0.8971	6.96	22.03	0.9286	5.85	23.55	0.9424
	RegNeRF [36]	20.44	13.59	0.8476	20.72	13.41	0.8418	19.70	13.68	0.8517
	FreeNeRF [72]	16.83	13.71	0.8534	6.84	22.26	0.9332	5.51	27.66	0.9485
	SparseNeRF [60]	17.76	12.83	0.8454	19.74	13.42	0.8316	21.56	14.36	0.8235
	ZeroRF [49]	19.88	14.17	0.8188	8.31	24.14	0.9211	5.34	27.78	0.9460
	FSGS [81]	9.51	21.07	0.9097	7.69	22.68	0.9264	6.06	25.31	0.9397
	GaussianObject (Ours)	4.98	24.81	0.9350	3.63	27.00	0.9512	2.75	28.62	0.9638
OmniObject3D	DVGO [58]	14.48	17.14	0.8952	12.89	18.32	0.9142	11.49	19.26	0.9302
	3DGS [22]	8.60	17.29	0.9299	7.74	18.29	0.9378	6.50	20.26	0.9483
	DietNeRF [18]	11.64	18.56	0.9205	10.39	19.07	0.9267	10.32	19.26	0.9258
	RegNeRF [36]	16.75	15.20	0.9091	14.38	15.80	0.9207	10.17	17.93	0.9420
	FreeNeRF [72]	8.28	17.78	0.9402	7.32	19.02	0.9464	7.25	20.35	0.9467
	SparseNeRF [60]	17.47	15.22	0.8921	21.71	15.86	0.8935	23.76	17.16	0.8947
	ZeroRF [49]	4.44	27.78	0.9615	3.11	31.94	0.9731	3.10	32.93	0.9747
	FSGS [81]	6.25	24.71	0.9545	6.05	26.36	0.9582	4.17	29.16	0.9695
	GaussianObject (Ours)	2.07	30.89	0.9756	1.55	33.31	0.9821	1.20	35.49	0.9870

Table 2. Quantitative comparisons on the OpenIllumination dataset. Methods with †means the metrics are from the ZeroRF paper [49].

Method	4-view			6-view		
	LPIPS* ↓	**PSNR** ↑	**SSIM** ↑	**LPIPS*** ↓	**PSNR** ↑	**SSIM** ↑
DVGO	11.84	21.15	0.8973	8.83	23.79	0.9209
3DGS	30.08	11.50	0.8454	29.65	11.98	0.8277
DietNeRF†	10.66	23.09	0.9361	9.51	24.20	0.9401
RegNeRF†	47.31	11.61	0.6940	30.28	14.08	0.8586
FreeNeRF†	35.81	12.21	0.7969	35.15	11.47	0.8128
SparseNeRF	22.28	13.60	0.8808	26.30	12.80	0.8403
ZeroRF†	9.74	24.54	0.9308	7.96	26.51	0.9415
Ours	6.71	24.64	0.9354	5.44	26.54	0.9443

Fig. 6. Qualitative results on the OpenIllumination dataset. Although ZeroRF shows competitive PSNR and SSIM, its renderings often appear blurred. While GaussianObject outperforms in restoring fine details, thereby achieving a significant advantage in perceptual quality.

Table 1 and Table 2 present the view-synthesis performance of GaussianObject compared to existing methods on the MipNeRF360, OmniObject3D, and OpenIllumination datasets. Experiments show that GaussianObject consistently achieves state-of-the-art results across all datasets, especially in the perceptual quality – LPIPS. Although GaussianObject is designed to address extremely sparse input views, it still outperforms other methods with more input views, *e.g.* 6 and 9, further proving the effectiveness. Notably, GaussianObject excels with as few as 4 views and significantly improves LPIPS over FSGS from 0.0951 to 0.0498 on MipNeRF360. This improvement is critical, as LPIPS is a key indicator of perceptual quality [37].

Fig. 5 and Fig. 6 illustrate rendering results of various methods across different datasets with only 4 input views. We observe that GaussianObject achieves significantly better visual quality and fidelity compared to the competing models. Notably, We find that implicit representation-based methods and random initialized 3DGS fail in extremely sparse settings, typically reconstructing objects as fragmented pixel patches. This confirms the effectiveness of integrating structure priors with explicit representations. Although ZeroRF exhibits competitive PSNR and SSIM on OpenIllumination, we observe that its renderings are blurred and lack details, as shown in Fig. 6. In contrast, GaussianObject demonstrates fine-detailed reconstruction. This superior perceptual quality highlights the effectiveness of the Gaussian repair model. It is highly suggested to refer to comprehensive video comparisons included in the supplementary.

4.4 Ablation Studies

Key Components We conduct a series of experiments to validate the effectiveness of each component. The following experiments are performed on MipNeRF360 with 4 input views and averaged

Table 3. Ablation study on key components.

Method	LPIPS* ↓	PSNR ↑	SSIM ↑
Ours w/o Visual Hull	12.72	15.95	0.8719
Ours w/o Floater Elimination	4.99	24.73	0.9346
Ours w/o Gaussian Repair	5.55	24.37	0.9297
Ours w/ SDS [38]	6.07	22.42	0.9188
GaussianObject (Ours)	**4.98**	**24.81**	**0.9350**

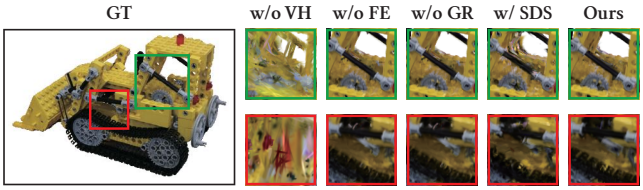

Fig. 7. Ablation study on different components. "VH" denotes for visual hull, "FE" is floater elimination and "GR" means Gaussian repair.

Table 4. Ablation study about alternatives of the Gaussian repair model.

Method	LPIPS* ↓	PSNR ↑	SSIM ↑
Dreambooth [45]	6.58	21.85	0.9093
Depth Condition	7.00	21.87	0.9112
Depth Condition w/ Mask	6.87	21.92	0.9117
GaussianObject (Ours)	**5.79**	**23.55**	**0.9220**

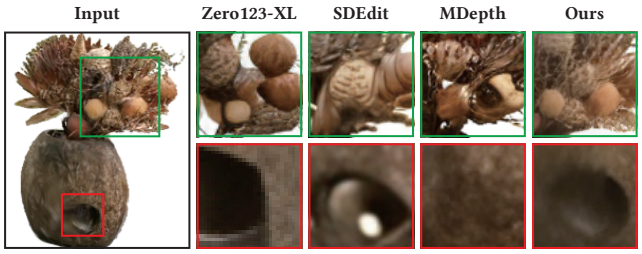

Fig. 8. Qualitative comparisons by ablating different Gaussian repair model alternatives. "MDepth" denotes the repair model with masked monocular depth estimation as the condition.

metric values are reported. We disable visual hull initialization, floater elimination and Gaussian repair once at a time to verify their effectiveness. The Gaussian repair loss is further compared with the Score Distillation Sampling (SDS) loss [38]. The results, presented in Table 3 and Fig. 7, indicate that each component significantly contributes to performance, with their absence leading to a decline in results. Particularly, omitting visual hull initialization results in a marked decrease in performance, while Gaussian repair markedly enhances perceptual quality. Contrary to its effectiveness in text-to-3D or single image-to-3D, SDS in our context results in unstable optimization and diminished performance.

Structure of Repair Model Our repair model is designed to generate photorealistic and 3D-consistent views of the target object. This is achieved by leave-one-out training and perturbing the attributes of 3D Gaussians to create image pairs for fine-tuning a pretrained image-conditioned ControlNet. Similarities can be found in Dreambooth [45], which aims to generate specific subject images from limited inputs. To validate the efficacy of our design, we evaluate the samples generated by our Gaussian repair model and other alternative structures. The first one is implemented with Dreambooth [45] for embedding target object priors with semantic modifications. The second one uses SDEdit [33] to guide the image generation. Inspired by Song et al. [55], the third one introduces a monocular depth conditioning ControlNet [75] which is finetuned using data pair generation as in Sec. 3.4. We also assess the performance using masked depth conditioning. Furthermore, we consider Zero123-XL [8, 29], a well-known single-image reconstruction model, requiring object-centered input images with precise camera rotations and positions. Here, we manually align the coordinate system and select the closest image to the novel viewpoint as its reference.

The results, as shown in Table 4 and Fig. 8, reveal that semantic modifications alone fail in 3D-coherent synthesis. Monocular depth conditioning, despite some improvements, still struggles with depth roughness and artifacts. Zero123-XL, while generating visually acceptable images, the multi-view structure consistency is lacking. In contrast, our model excels in both 3D consistency and detail fidelity, outperforming others qualitatively and quantitatively.

5 DISCUSSION AND CONCLUSION

Limitations & Future Work. GaussianObject demonstrates notable performance in sparse 360° object reconstruction, yet several avenues for future research exist, including reducing reliance on precise camera poses, mitigating popping artifacts in extreme views, and addressing color shifts in stable diffusion VAEs. The current dependency of GaussianObject on precise poses for visual hull construction and optimization raises challenges among daily life. A potential solution is to optimize camera parameters together with 3D reconstruction under specific capturing rules. Additionally, 3DGS-like methods occasionally exhibit popping artifacts under extreme viewpoints, affecting visual quality. Future work could explore anti-aliasing techniques or a more comprehensive repair path, such as a hemisphere repair path, to address this issue. Moreover, we observe consistent color shifts on white backgrounds due to the VAE of stable diffusion, which could potentially impact the Gaussian repair process. Training the repair model from a more powerful diffusion model may mitigate this issue.

In summary, GaussianObject is a novel framework designed for high-quality 3D object reconstruction from extremely sparse 360° views, based on 3DGS with real-time rendering capabilities. We design two main methods to achieve this goal: structure-prior-aided optimization for facilitating the multi-view consistency construction and a Gaussian repair model to remove artifacts caused by omitted or highly compressed object information. We hope that GaussianObject can advance daily-life applications of reconstructing 3D objects,

markedly reducing capture requirements and broadening application prospects.

REFERENCES

[1] Jonathan T. Barron, Ben Mildenhall, Dor Verbin, Pratul P. Srinivasan, and Peter Hedman. 2021. Mip-NeRF 360: Unbounded Anti-Aliased Neural Radiance Fields. *2022 IEEE/CVF Conference on Computer Vision and Pattern Recognition (CVPR)* (2021), 5460–5469. https://api.semanticscholar.org/CorpusID:244488448

[2] Shariq Farooq Bhat, Reiner Birkl, Diana Wofk, Peter Wonka, and Matthias Müller. 2023. Zoedepth: Zero-shot transfer by combining relative and metric depth. *arXiv preprint arXiv:2302.12288* (2023).

[3] Jiazhong Cen, Zanwei Zhou, Jiemin Fang, Chen Yang, Wei Shen, Lingxi Xie, Dongsheng Jiang, Xiaopeng Zhang, and Qi Tian. 2023. Segment Anything in 3D with NeRFs. In *NeurIPS*.

[4] Eric R Chan, Koki Nagano, Matthew A Chan, Alexander W Bergman, Jeong Joon Park, Axel Levy, Miika Aittala, Shalini De Mello, Tero Karras, and Gordon Wetzstein. 2023. GeNVS: Generative novel view synthesis with 3D-aware diffusion models.

[5] Jonathan Chang. 2023. minLoRA. https://github.com/cccntu/minLoRA.

[6] Rui Chen, Yongwei Chen, Ningxin Jiao, and Kui Jia. 2023. Fantasia3D: Disentangling Geometry and Appearance for High-quality Text-to-3D Content Creation. In *Proceedings of the IEEE/CVF International Conference on Computer Vision (ICCV)*. 22246–22256.

[7] Jaeyoung Chung, Jeongtaek Oh, and Kyoung Mu Lee. 2024. Depth-Regularized Optimization for 3D Gaussian Splatting in Few-Shot Images. arXiv:2311.13398 (Jan. 2024). https://doi.org/10.48550/arXiv.2311.13398

[8] Matt Deitke, Ruoshi Liu, Matthew Wallingford, Huong Ngo, Oscar Michel, Aditya Kusupati, Alan Fan, Christian Laforte, Vikram Voleti, Samir Yitzhak Gadre, Eli VanderBilt, Aniruddha Kembhavi, Carl Vondrick, Georgia Gkioxari, Kiana Ehsani, Ludwig Schmidt, and Ali Farhadi. 2023. Objaverse-XL: A Universe of 10M+ 3D Objects. *arXiv preprint arXiv:2307.05663* (2023).

[9] Kangle Deng, Andrew Liu, Jun-Yan Zhu, and Deva Ramanan. 2022. Depth-supervised NeRF: Fewer Views and Faster Training for Free. In *2022 IEEE/CVF Conference on Computer Vision and Pattern Recognition (CVPR)*. 12872–12881. https://doi.org/10.1109/CVPR52688.2022.01254

[10] Prafulla Dhariwal and Alexander Nichol. 2021. Diffusion Models Beat GANs on Image Synthesis. In *Advances in Neural Information Processing Systems*, M. Ranzato, A. Beygelzimer, Y. Dauphin, P.S. Liang, and J. Wortman Vaughan (Eds.), Vol. 34. Curran Associates, Inc., 8780–8794. https://proceedings.neurips.cc/paper_files/paper/2021/file/49ad23d1ec9fa4bd8d77d02681df5cfa-Paper.pdf

[11] Alexey Dosovitskiy, Lucas Beyer, Alexander Kolesnikov, Dirk Weissenborn, Xiaohua Zhai, Thomas Unterthiner, Mostafa Dehghani, Matthias Minderer, Georg Heigold, Sylvain Gelly, Jakob Uszkoreit, and Neil Houlsby. 2021. An Image is Worth 16x16 Words: Transformers for Image Recognition at Scale. In *International Conference on Learning Representations*. https://openreview.net/forum?id=YicbFdNTTy

[12] Shuyang Gu, Dong Chen, Jianmin Bao, Fang Wen, Bo Zhang, Dongdong Chen, Lu Yuan, and Baining Guo. 2022. Vector Quantized Diffusion Model for Text-to-Image Synthesis. In *2022 IEEE/CVF Conference on Computer Vision and Pattern Recognition (CVPR)*. 10686–10696. https://doi.org/10.1109/CVPR52688.2022.01043

[13] Yuan-Chen Guo, Ying-Tian Liu, Ruizhi Shao, Christian Laforte, Vikram Voleti, Guan Luo, Chia-Hao Chen, Zi-Xin Zou, Chen Wang, Yan-Pei Cao, and Song-Hai Zhang. 2023. threestudio: A unified framework for 3D content generation. https://github.com/threestudio-project/threestudio.

[14] Ayaan Haque, Matthew Tancik, Alexei Efros, Aleksander Holynski, and Angjoo Kanazawa. 2023. Instruct-NeRF2NeRF: Editing 3D Scenes with Instructions. In *Proceedings of the IEEE/CVF International Conference on Computer Vision*.

[15] Jonathan Ho, Ajay Jain, and Pieter Abbeel. 2020. Denoising diffusion probabilistic models. *Advances in neural information processing systems* 33 (2020), 6840–6851.

[16] Yicong Hong, Kai Zhang, Jiuxiang Gu, Sai Bi, Yang Zhou, Difan Liu, Feng Liu, Kalyan Sunkavalli, Trung Bui, and Hao Tan. 2023. Lrm: Large reconstruction model for single image to 3d. *arXiv preprint arXiv:2311.04400* (2023).

[17] Edward J Hu, Yelong Shen, Phillip Wallis, Zeyuan Allen-Zhu, Yuanzhi Li, Shean Wang, Lu Wang, and Weizhu Chen. 2021. Lora: Low-rank adaptation of large language models. *arXiv preprint arXiv:2106.09685* (2021).

[18] Ajay Jain, Matthew Tancik, and Pieter Abbeel. 2021. Putting NeRF on a Diet: Semantically Consistent Few-Shot View Synthesis. In *2021 IEEE/CVF International Conference on Computer Vision (ICCV)*. 5865–5874. https://doi.org/10.1109/ICCV48922.2021.00583

[19] Wonbong Jang and Lourdes Agapito. 2023. NViST: In the Wild New View Synthesis from a Single Image with Transformers. (2023). arXiv:2312.08568 [cs.CV]

[20] Hanwen Jiang, Zhenyu Jiang, Yue Zhao, and Qixing Huang. 2023. LEAP: Liberate Sparse-view 3D Modeling from Camera Poses. *arXiv preprint arXiv:2310.01410* (2023).

[21] Tero Karras, Miika Aittala, Timo Aila, and Samuli Laine. 2022. Elucidating the Design Space of Diffusion-Based Generative Models. In *Proc. NeurIPS*.

[22] Bernhard Kerbl, Georgios Kopanas, Thomas Leimkühler, and George Drettakis. 2023. 3D Gaussian Splatting for Real-Time Radiance Field Rendering. *ACM Transactions on Graphics* 42, 4 (2023).

[23] Mijeong Kim, Seonguk Seo, and Bohyung Han. 2022. Infonerf: Ray entropy minimization for few-shot neural volume rendering. In *Proceedings of the IEEE/CVF Conference on Computer Vision and Pattern Recognition*. 12912–12921.

[24] Diederik P. Kingma and Max Welling. 2014. Auto-Encoding Variational Bayes. In *2nd International Conference on Learning Representations, ICLR 2014, Banff, AB, Canada, April 14-16, 2014, Conference Track Proceedings*, Yoshua Bengio and Yann LeCun (Eds.). http://arxiv.org/abs/1312.6114

[25] Alexander Kirillov, Eric Mintun, Nikhila Ravi, Hanzi Mao, Chloe Rolland, Laura Gustafson, Tete Xiao, Spencer Whitehead, Alexander C Berg, Wan-Yen Lo, et al. 2023. Segment anything. *arXiv preprint arXiv:2304.02643* (2023).

[26] A. Laurentini. 1994. The visual hull concept for silhouette-based image understanding. *IEEE Transactions on Pattern Analysis and Machine Intelligence* 16, 2 (1994), 150–162. https://doi.org/10.1109/34.273735

[27] Chen-Hsuan Lin, Jun Gao, Luming Tang, Towaki Takikawa, Xiaohui Zeng, Xun Huang, Karsten Kreis, Sanja Fidler, Ming-Yu Liu, and Tsung-Yi Lin. 2023. Magic3D: High-Resolution Text-to-3D Content Creation. In *IEEE Conference on Computer Vision and Pattern Recognition (CVPR)*.

[28] Isabella Liu, Linghao Chen, Ziyang Fu, Liwen Wu, Haian Jin, Zhong Li, Chin Ming Ryan Wong, Yi Xu, Ravi Ramamoorthi, Zexiang Xu, and Hao Su. 2023. OpenIllumination: A Multi-Illumination Dataset for Inverse Rendering Evaluation on Real Objects. *NeuRIPS 2023*.

[29] Ruoshi Liu, Rundi Wu, Basile Van Hoorick, Pavel Tokmakov, Sergey Zakharov, and Carl Vondrick. 2023. Zero-1-to-3: Zero-shot One Image to 3D Object. In *Proceedings of the IEEE/CVF International Conference on Computer Vision (ICCV)*. 9298–9309.

[30] Xinhang Liu, Shiu-hong Kao, Jiaben Chen, Yu-Wing Tai, and Chi-Keung Tang. 2023. Deceptive-NeRF: Enhancing NeRF Reconstruction using Pseudo-Observations from Diffusion Models. *arXiv preprint arXiv:2305.15171* (2023).

[31] Ilya Loshchilov and Frank Hutter. 2019. Decoupled Weight Decay Regularization. In *International Conference on Learning Representations*. https://openreview.net/forum?id=Bkg6RiCqY7

[32] Cheng Lu, Yuhao Zhou, Fan Bao, Jianfei Chen, Chongxuan LI, and Jun Zhu. 2022. DPM-Solver: A Fast ODE Solver for Diffusion Probabilistic Model Sampling in Around 10 Steps. In *Advances in Neural Information Processing Systems*, S. Koyejo, S. Mohamed, A. Agarwal, D. Belgrave, K. Cho, and A. Oh (Eds.), Vol. 35. Curran Associates, Inc., 5775–5787. https://proceedings.neurips.cc/paper_files/paper/2022/file/260a14acce2a89dad36adc8eefe7c59e-Paper-Conference.pdf

[33] Chenlin Meng, Yutong He, Yang Song, Jiaming Song, Jiajun Wu, Jun-Yan Zhu, and Stefano Ermon. 2021. Sdedit: Guided image synthesis and editing with stochastic differential equations. *arXiv preprint arXiv:2108.01073* (2021).

[34] Gal Metzer, Elad Richardson, Or Patashnik, Raja Giryes, and Daniel Cohen-Or. 2023. Latent-NeRF for Shape-Guided Generation of 3D Shapes and Textures. In *2023 IEEE/CVF Conference on Computer Vision and Pattern Recognition (CVPR)*. 12663–12673. https://doi.org/10.1109/CVPR52729.2023.01218

[35] Ben Mildenhall, Pratul P. Srinivasan, Matthew Tancik, Jonathan T. Barron, Ravi Ramamoorthi, and Ren Ng. 2020. NeRF: Representing Scenes as Neural Radiance Fields for View Synthesis. In *ECCV (Lecture Notes in Computer Science, Vol. 12346)*. Springer, 405–421. https://doi.org/10.1007/978-3-030-58452-8_24

[36] Michael Niemeyer, Jonathan T. Barron, Ben Mildenhall, Mehdi S. M. Sajjadi, Andreas Geiger, and Noha Radwan. 2022. RegNeRF: Regularizing Neural Radiance Fields for View Synthesis from Sparse Inputs. In *2022 IEEE/CVF Conference on Computer Vision and Pattern Recognition (CVPR)*. 5470–5480. https://doi.org/10.1109/CVPR52688.2022.00540

[37] Keunhong Park, Utkarsh Sinha, Peter Hedman, Jonathan T Barron, Sofien Bouaziz, Dan B Goldman, Ricardo Martin-Brualla, and Steven M Seitz. 2021. Hypernerf: A higher-dimensional representation for topologically varying neural radiance fields. *arXiv preprint arXiv:2106.13228* (2021).

[38] Ben Poole, Ajay Jain, Jonathan T Barron, and Ben Mildenhall. 2022. Dreamfusion: Text-to-3d using 2d diffusion. *arXiv preprint arXiv:2209.14988* (2022).

[39] Alec Radford, Jong Wook Kim, Chris Hallacy, Aditya Ramesh, Gabriel Goh, Sandhini Agarwal, Girish Sastry, Amanda Askell, Pamela Mishkin, Jack Clark, Gretchen Krueger, and Ilya Sutskever. 2021. Learning Transferable Visual Models From Natural Language Supervision. In *Proceedings of the 38th International Conference on Machine Learning*. PMLR, 8748–8763. https://proceedings.mlr.press/v139/radford21a.html

[40] René Ranftl, Alexey Bochkovskiy, and Vladlen Koltun. 2021. Vision Transformers for Dense Prediction. *ICCV* (2021).

[41] René Ranftl, Katrin Lasinger, David Hafner, Konrad Schindler, and Vladlen Koltun. 2020. Towards robust monocular depth estimation: Mixing datasets for zero-shot cross-dataset transfer. *IEEE transactions on pattern analysis and machine intelligence* 44, 3 (2020), 1623–1637.

[42] René Ranftl, Katrin Lasinger, David Hafner, Konrad Schindler, and Vladlen Koltun. 2022. Towards Robust Monocular Depth Estimation: Mixing Datasets for Zero-Shot Cross-Dataset Transfer. *IEEE Transactions on Pattern Analysis and Machine Intelligence* 44, 3 (2022).

[43] Barbara Roessle, Jonathan T Barron, Ben Mildenhall, Pratul P Srinivasan, and Matthias Nießner. 2022. Dense depth priors for neural radiance fields from sparse input views. In *Proceedings of the IEEE/CVF Conference on Computer Vision and Pattern Recognition*. 12892–12901.

[44] Robin Rombach, Andreas Blattmann, Dominik Lorenz, Patrick Esser, and Björn Ommer. 2022. High-Resolution Image Synthesis with Latent Diffusion Models. In *2022 IEEE/CVF Conference on Computer Vision and Pattern Recognition (CVPR)*. 10674–10685. https://doi.org/10.1109/CVPR52688.2022.01042

[45] Nataniel Ruiz, Yuanzhen Li, Varun Jampani, Yael Pritch, Michael Rubinstein, and Kfir Aberman. 2023. Dreambooth: Fine tuning text-to-image diffusion models for subject-driven generation. In *Proceedings of the IEEE/CVF Conference on Computer Vision and Pattern Recognition*. 22500–22510.

[46] Johannes Lutz Schönberger and Jan-Michael Frahm. 2016. Structure-from-Motion Revisited. In *Conference on Computer Vision and Pattern Recognition (CVPR)*.

[47] Seunghyeon Seo, Yeonjin Chang, and Nojun Kwak. 2023. Flipnerf: Flipped reflection rays for few-shot novel view synthesis. In *Proceedings of the IEEE/CVF International Conference on Computer Vision*. 22883–22893.

[48] Ruizhi Shao, Jingxiang Sun, Cheng Peng, Zerong Zheng, Boyao Zhou, Hongwen Zhang, and Yebin Liu. 2023. Control4D: Efficient 4D Portrait Editing with Text. (2023).

[49] Ruoxi Shi, Xinyue Wei, Cheng Wang, and Hao Su. 2023. ZeroRF: Fast Sparse View 360° Reconstruction with Zero Pretraining. *CoRR* abs/2312.09249 (2023). https://doi.org/10.48550/ARXIV.2312.09249 arXiv:2312.09249

[50] Yichun Shi, Peng Wang, Jianglong Ye, Long Mai, Kejie Li, and Xiao Yang. 2023. MVDream: Multi-view Diffusion for 3D Generation. *arXiv:2308.16512* (2023).

[51] Jascha Sohl-Dickstein, Eric Weiss, Niru Maheswaranathan, and Surya Ganguli. 2015. Deep Unsupervised Learning using Nonequilibrium Thermodynamics. In *Proceedings of the 32nd International Conference on Machine Learning (Proceedings of Machine Learning Research, Vol. 37)*, Francis Bach and David Blei (Eds.). PMLR, Lille, France, 2256–2265. https://proceedings.mlr.press/v37/sohl-dickstein15.html

[52] Nagabhushan Somraj, Adithyan Karanayil, and Rajiv Soundararajan. 2023. SimpleNeRF: Regularizing Sparse Input Neural Radiance Fields with Simpler Solutions. In *SIGGRAPH Asia 2023 Conference Papers (SA '23)*. Association for Computing Machinery, New York, NY, USA, 1–11. https://doi.org/10.1145/3610548.3618188

[53] Nagabhushan Somraj and Rajiv Soundararajan. 2023. ViP-NeRF: Visibility Prior for Sparse Input Neural Radiance Fields. (August 2023). https://doi.org/10.1145/3588432.3591539

[54] Jiaming Song, Chenlin Meng, and Stefano Ermon. 2020. Denoising diffusion implicit models. *arXiv preprint arXiv:2010.02502* (2020).

[55] Jiuhn Song, Seonghoon Park, Honggyu An, Seokju Cho, Min-Seop Kwak, Sungjin Cho, and Seungryong Kim. 2023. DaRF: Boosting Radiance Fields from Sparse Inputs with Monocular Depth Adaptation. arXiv:2305.19201 (Sept. 2023). https://doi.org/10.48550/arXiv.2305.19201 arXiv:2305.19201 [cs].

[56] Yang Song and Stefano Ermon. 2019. Generative Modeling by Estimating Gradients of the Data Distribution. In *Advances in Neural Information Processing Systems*, H. Wallach, H. Larochelle, A. Beygelzimer, F. d'Alché-Buc, E. Fox, and R. Garnett (Eds.), Vol. 32. Curran Associates, Inc. https://proceedings.neurips.cc/paper_files/paper/2019/file/3001ef257407d5a371a96dcd947c7d93-Paper.pdf

[57] Yang Song, Jascha Sohl-Dickstein, Diederik P Kingma, Abhishek Kumar, Stefano Ermon, and Ben Poole. 2021. Score-Based Generative Modeling through Stochastic Differential Equations. In *International Conference on Learning Representations*. https://openreview.net/forum?id=PxTIG12RRHS

[58] Cheng Sun, Min Sun, and Hwann-Tzong Chen. 2022. Direct Voxel Grid Optimization: Super-fast Convergence for Radiance Fields Reconstruction. In *CVPR*.

[59] Jiaxiang Tang, Jiawei Ren, Hang Zhou, Ziwei Liu, and Gang Zeng. 2023. DreamGaussian: Generative Gaussian Splatting for Efficient 3D Content Creation. *arXiv preprint arXiv:2309.16653* (2023).

[60] Guangcong Wang, Zhaoxi Chen, Chen Change Loy, and Ziwei Liu. 2023. SparseNeRF: Distilling Depth Ranking for Few-shot Novel View Synthesis. arXiv:2303.16196 (Aug. 2023). https://doi.org/10.48550/arXiv.2303.16196 arXiv:2303.16196 [cs].

[61] Haochen Wang, Xiaodan Du, Jiahao Li, Raymond A. Yeh, and Greg Shakhnarovich. 2023. Score Jacobian Chaining: Lifting Pretrained 2D Diffusion Models for 3D Generation. In *2023 IEEE/CVF Conference on Computer Vision and Pattern Recognition (CVPR)*. 12619–12629. https://doi.org/10.1109/CVPR52729.2023.01214

[62] Peng Wang, Hao Tan, Sai Bi, Yinghao Xu, Fujun Luan, Kalyan Sunkavalli, Wenping Wang, Zexiang Xu, and Kai Zhang. 2023. PF-LRM: Pose-Free Large Reconstruction Model for Joint Pose and Shape Prediction. *arXiv preprint arXiv:2311.12024* (2023).

[63] Zhengyi Wang, Cheng Lu, Yikai Wang, Fan Bao, Chongxuan Li, Hang Su, and Jun Zhu. 2023. ProlificDreamer: High-Fidelity and Diverse Text-to-3D Generation with Variational Score Distillation. In *Advances in Neural Information Processing Systems (NeurIPS)*.

[64] Olivia Wiles, Georgia Gkioxari, Richard Szeliski, and Justin Johnson. 2020. SynSin: End-to-end View Synthesis from a Single Image. In *CVPR*.

[65] Rundi Wu, Ben Mildenhall, Philipp Henzler, Keunhong Park, Ruiqi Gao, Daniel Watson, Pratul P Srinivasan, Dor Verbin, Jonathan T Barron, Ben Poole, et al. 2023. ReconFusion: 3D Reconstruction with Diffusion Priors. *arXiv preprint arXiv:2312.02981* (2023).

[66] Tong Wu, Jiarui Zhang, Xiao Fu, Yuxin Wang, Jiawei Ren, Liang Pan, Wayne Wu, Lei Yang, Jiaqi Wang, Chen Qian, Dahua Lin, and Ziwei Liu. 2023. OmniObject3D: Large-Vocabulary 3D Object Dataset for Realistic Perception, Reconstruction and Generation. *2023 IEEE/CVF Conference on Computer Vision and Pattern Recognition (CVPR)* (2023), 803–814. https://api.semanticscholar.org/CorpusID:255998491

[67] Jamie Wynn and Daniyar Turmukhambetov. 2023. DiffusioNeRF: Regularizing Neural Radiance Fields with Denoising Diffusion Models. In *2023 IEEE/CVF Conference on Computer Vision and Pattern Recognition (CVPR)*. 4180–4189. https://doi.org/10.1109/CVPR52729.2023.00407

[68] Haolin Xiong, Sairisheek Muttukuru, Rishi Upadhyay, Pradyumna Chari, and Achuta Kadambi. 2023. SparseGS: Real-Time 360° Sparse View Synthesis using Gaussian Splatting. arXiv:2312.00206 (Nov. 2023). https://doi.org/10.48550/arXiv.2312.00206

[69] Dejia Xu, Yifan Jiang, Peihao Wang, Zhiwen Fan, Humphrey Shi, and Zhangyang Wang. 2022. SinNeRF: Training Neural Radiance Fields on Complex Scenes from a Single Image. In *Computer Vision – ECCV 2022 (Lecture Notes in Computer Science)*, Shai Avidan, Gabriel Brostow, Moustapha Cissé, Giovanni Maria Farinella, and Tal Hassner (Eds.). Springer Nature Switzerland, Cham, 736–753. https://doi.org/10.1007/978-3-031-20047-2_42

[70] Qiangeng Xu, Zexiang Xu, Julien Philip, Sai Bi, Zhixin Shu, Kalyan Sunkavalli, and Ulrich Neumann. 2022. Point-nerf: Point-based neural radiance fields. In *Proceedings of the IEEE/CVF Conference on Computer Vision and Pattern Recognition*. 5438–5448.

[71] Yinghao Xu, Hao Tan, Fujun Luan, Sai Bi, Peng Wang, Jiahao Li, Zifan Shi, Kalyan Sunkavalli, Gordon Wetzstein, Zexiang Xu, and Kai Zhang. 2023. DMV3D: Denoising Multi-View Diffusion using 3D Large Reconstruction Model. arXiv:2311.09217 [cs.CV]

[72] Jiawei Yang, Marco Pavone, and Yue Wang. 2023. FreeNeRF: Improving Few-Shot Neural Rendering with Free Frequency Regularization. In *2023 IEEE/CVF Conference on Computer Vision and Pattern Recognition (CVPR)*. 8254–8263. https://doi.org/10.1109/CVPR52729.2023.00798

[73] Taoran Yi, Jiemin Fang, Junjie Wang, Guanjun Wu, Lingxi Xie, Xiaopeng Zhang, Wenyu Liu, Qi Tian, and Xinggang Wang. 2023. GaussianDreamer: Fast Generation from Text to 3D Gaussians by Bridging 2D and 3D Diffusion Models. *arXiv preprint arXiv:2310.08529* (2023).

[74] Wang Yifan, Felice Serena, Shihao Wu, Cengiz Öztireli, and Olga Sorkine-Hornung. 2019. Differentiable Surface Splatting for Point-based Geometry Processing. *ACM Transactions on Graphics (proceedings of ACM SIGGRAPH ASIA)* 38, 6 (2019).

[75] Lvmin Zhang, Anyi Rao, and Maneesh Agrawala. 2023. Adding conditional control to text-to-image diffusion models. In *Proceedings of the IEEE/CVF International Conference on Computer Vision*. 3836–3847.

[76] Lvmin Zhang, Anyi Rao, and Maneesh Agrawala. 2023. ControlNet-v1-1-nightly. https://github.com/lllyasviel/ControlNet-v1-1-nightly.

[77] Qiang Zhang, Seung-Hwan Baek, Szymon Rusinkiewicz, and Felix Heide. 2022. Differentiable Point-Based Radiance Fields for Efficient View Synthesis. In *SIGGRAPH Asia 2022 Conference Papers (SA '22)*. Association for Computing Machinery, New York, NY, USA, Article 7, 12 pages.

[78] Richard Zhang, Phillip Isola, Alexei A Efros, Eli Shechtman, and Oliver Wang. 2018. The unreasonable effectiveness of deep features as a perceptual metric. In *Proceedings of the IEEE conference on computer vision and pattern recognition*. 586–595.

[79] Zhizhuo Zhou and Shubham Tulsiani. 2023. SparseFusion: Distilling View-Conditioned Diffusion for 3D Reconstruction. In *2023 IEEE/CVF Conference on Computer Vision and Pattern Recognition (CVPR)*. 12588–12597. https://doi.org/10.1109/CVPR52729.2023.01211

[80] Junzhe Zhu and Peiye Zhuang. 2023. HiFA: High-fidelity Text-to-3D Generation with Advanced Diffusion Guidance. arXiv:2305.18766 [cs.CV]

[81] Zehao Zhu, Zhiwen Fan, Yifan Jiang, and Zhangyang Wang. 2023. FSGS: Real-Time Few-shot View Synthesis using Gaussian Splatting. *arXiv preprint arXiv:2312.00451* (2023).

[82] Zi-Xin Zou, Zhipeng Yu, Yuan-Chen Guo, Yangguang Li, Ding Liang, Yan-Pei Cao, and Song-Hai Zhang. 2023. Triplane Meets Gaussian Splatting: Fast and Generalizable Single-View 3D Reconstruction with Transformers. arXiv:2312.09147 [cs.CV]

A APPENDIX

A.1 Dataset Details

MipNeRF360. The sparse MipNeRF360 dataset, derived from the dataset provided by [1], focuses on three scenes containing a primary object: bonsai, garden, and kitchen. We employ [3] to extract the plastic bonsai, the flower pot and the Lego bulldozer from the original scenes. For performance evaluation, the scenes are tested using images downsampled by a factor of 4×, following the train-test splits from [65].

OmniObject3D. OmniObject3D includes 6k real 3D objects in 190 large-vocabulary categories. We selected 17 objects from OmniObject3D [66] and generated their masks using [3]. The items chosen include: *back-pack_016*, *box_043*, *broccoli_003*, *corn_007*, *dinosaur_006*, *flower_pot_007*, *gloves_009*, *guitar_002*, *hamburger_012*, *picnic_basket_009*, *pineapple_013*, *sandwich_003*, *suitcase_006*, *timer_010*, *toy_plane_005*, *toy_truck_037*, and *vase_012* for a fair evaluation. We manually choose camera views for training, and use every eighth view left for testing. Most scenes are originally in 1080p resolution, while *gloves_009* and *timer_010* are in 720p resolution. To maintain consistency across all scenes, we upscaled the images from these two scenes to 1080p resolution. All the images are downsampled to a factor of 2×.

OpenIllumination. OpenIllumination is a real-world dataset captured by the LightStage. We use the sparse OpenIllumination dataset proposed in ZeroRF [49]. Note that ZeroRF re-scaled and re-centered the camera poses to align the target object with the world center. We test on the sparse OpenIllumination dataset [28] with provided object masks and train-test splits, downscaling the images by a factor of 4×, following the same experimental setting as in [49].

A.2 Implement Details

We build our GaussianObject upon 3DGS [22] and Threestudio [13]. For visual hull reconstruction, we adopt a coarse-to-fine approach: starting with rough spatial sampling to estimate the bounding box, then proceeding to detailed sampling within it. Since the sparse input views cannot provide sufficient multi-view consistency, we reconstruct all objects with only two degrees of spherical harmonics (SH). As for floater elimination, we start it from 500 iterations and conduct it every 500 iterations until 6k iterations. The adaptive threshold τ is initially set to the mean plus the standard deviation of the average distance calculated via KNN, and is linearly decreased to 0 in 6k iterations. The loss weight for $\mathcal{L}_{\text{gs}}$ is set to: $\lambda_{\text{SSIM}} = 0.2$, $\lambda_{\text{m}} = 0.001$ and $\mathcal{L}_{\text{d}} = 0.0005$.

For the Gaussian repair model setup, we use leave-one-out training to generate image pairs and 3D Noise ϵ_s. We use the visual hull corresponding to N reference images as initialization of all 3DGS models during leave-one-out training. We add noises to all the attributes of 3D Gaussians except for SH coefficients. Every time we need a data pair from adding 3D noises, we use the mean μ_Δ and variance σ_Δ to generate new noisy Gaussians for rendering, thus enabling sufficient data generation. All the images are constant padded or center croped before fed into the Gaussian repair model to preserve the real ratio of target object. At the first iteration of training the Gaussian repair model, manual noise generated according to a distribution is used for training with a 100% probability. Each time training is conducted with manual noise, this probability is reduced by 0.5%, to increasingly utilize cached images from leave-one-out training. The [V] used for object-specific text prompt is "xxy5syt00".

For the Gaussian repair process, we optimize the coarse 3DGS model for 4k steps, with first 2800 steps supervised by $\mathcal{L}_{\text{rep}}$ and $\mathcal{L}_{\text{gs}}$ together. Based on the camera poses of N reference views, we estimate an elliptic trajectory that encircles the object, and find N points on the trajectory that are respectively the closest to the reference views. These N points divide the ellipse into N segments of arc. On each segment of the arc, novel views are only sampled from the middle 80% of the arc (repair path), the remaining arcs constitute reference paths. To expedite training, we avoid using the time-consuming DDIM process [54] for every novel view rendering. Instead, we employ cached images for optimization. Specifically, at the beginning of every 200 iterations, we sample and repair two novel views from each repair path. Throughout these 200 iterations, we utilize these images to repair 3D Gaussians. We set the weights for $\mathcal{L}_{\text{rep}}$ as follows: $\lambda_1 = 0.5$, $\lambda_2 = 0.5$ and $\lambda_p = 2.0$ accross all experiments. We employ densification and opacity resetting to regulate the number of Gaussians. The Gaussian densification process is effective from 400 to 3600 steps. The Gaussian model undergoes densification and pruning at intervals of every 100 steps, and its opacity is reset every 500 steps.

A.3 Experiment Details

FSGS [81] requires SfM points generated from the input images, which are too sparse in our setting of 4 input views. Alternatively, we randomly pick N_{pick} points from the SfM points with full images as input:

$$N_{\text{pick}} = \max\left(150, \frac{k_{\text{sparse}}}{k_{\text{all}}} N_{\text{all}}\right), \tag{13}$$

where k_{sparse} is the number of input images, k_{all} is the toatl number of images, and N_{all} is the total number of points.

A.4 More Experimental Results

We provide per-scene qualitative metrics of MipNeRF360 in Tab. 5, Tab. 6 and Tab. 7; of OmniObject3D in Tab. 8, Tab. 9, Tab. 10, Tab. 11, Tab. 12 and Tab. 13; of OpenIllumination in Tab. 14 and Tab. 15. Additional qualitative comparisons on OpenIllumination dataset are shown in Fig. 10.

Furthermore, We provide extra validations on our Gaussian repair process. Figure 9 illustrates both the distribution of coarse 3D Gaussians and the refined distribution after the Gaussian repair. This comparison clearly demonstrates the significant enhancement in geometry achieved by our repair process. We also provide qualitative samples of the Gaussian repair model in Fig. 11, showing that the Gaussian repair model can effectively generate high-quality and consistent images from multiple views.

A.5 Abaltion Study Details

We employ ControlNet-Tile [75, 76] as the Gaussian repair model of GaussianObject. ControlNet-Tile, based on Stable Diffusion v1.5, is designed to repair low-resolution or low-fidelity images by taking them as conditions. In our ablation study, we use other diffusion

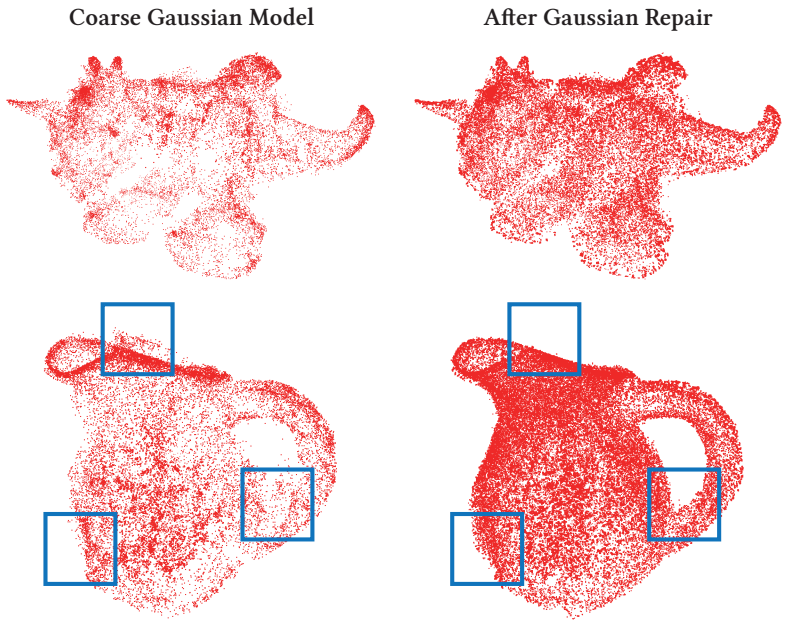

Fig. 9. Point clouds of GaussianObject before and after Gaussian repair. In the *dinosaur* scene, the Gaussian repair model significantly enhances the point cloud density, resulting in a more distinct and clear representation of the dinosaur's body. In the *vase* scene, noticeable artifacts around the handle and the mouth are effectively eliminated by the Gaussian repair model, and the incomplete bottom of the vase is repaired. These key areas are highlighted with blue boxes.

models serving as our Gaussian repair model in Sec.4.4. First, we use Stable Diffusion XL Image-to-Image [33], which cannot directly take images as input conditions. Therefore, we add 50% Gaussian noise to the novel view images and use the model to generate high-fidelity images by denoising the noisy images. Additionally, we evaluate ControlNet-ZoeDepth, based on Stable Diffusion XL. ControlNet-ZoeDepth, which takes the ZoeDepth [2] as a condition, is used to generate images aligned with the depth map. However, ZoeDepth may incorrectly assume that a single object with a white background is on a white table, leading to erroneous depth map predictions. In such cases, we test two settings: one using the entire predicted depth map and another using the object-masked depth map. Due to the ambiguity of monocular predicted depth, we add partial noise on the input image to preserve the image information, similar to SDEdit. Specifically, we add 50% Gaussian noise to the novel view images and set the weight scale of the ControlNet model to 0.55. In this experimental setup, we obtained the results of the ablation experiments on the structure of the Gaussian repair model.

Fig. 10. Qualitative examples on the OpenIllumination dataset with four input views.

Fig. 11. Qualitative samples of the Gaussian repaired models on several scenes from different views.

Table 5. Comparisons of per-scene metrics of MipNeRF360 with 4 input views.

Method	bonsai			garden			kitchen		
	LPIPS ↓	PSNR ↑	SSIM ↑	LPIPS ↓	PSNR ↑	SSIM ↑	LPIPS ↓	PSNR ↑	SSIM ↑
DVGO [58]	0.3324	10.45	0.6980	0.0559	21.75	0.9652	0.3447	10.97	0.7104
3DGS [22]	0.1408	16.42	0.8458	0.0417	26.05	0.9769	0.1414	18.47	0.8746
DietNeRF [18]	0.1333	16.30	0.8682	0.0231	28.63	0.9780	0.1787	11.77	0.8453
RegNeRF [36]	0.2736	9.99	0.7847	0.0300	20.89	0.9794	0.3094	9.89	0.7788
FreeNeRF [72]	0.2172	10.16	0.8052	0.0300	20.89	0.9760	0.2578	10.08	0.7789
SparseNeRF [60]	0.2148	10.08	0.8037	0.0618	18.36	0.9556	0.2562	10.04	0.7769
ZeroRF [49]	0.2206	10.36	0.7810	0.0434	22.52	0.9596	0.3324	9.62	0.7157
FSGS [81]	0.1258	17.96	0.8707	0.0279	25.84	0.9766	0.1317	19.40	0.8818
GaussianObject	0.0690	21.51	0.9113	0.0121	30.56	0.9833	0.0687	22.36	0.9104

Table 6. Comparisons of per-scene metrics of MipNeRF360 with 6 input views.

Method	bonsai			garden			kitchen		
	LPIPS ↓	PSNR ↑	SSIM ↑	LPIPS ↓	PSNR ↑	SSIM ↑	LPIPS ↓	PSNR ↑	SSIM ↑
DVGO [58]	0.3908	10.11	0.6531	0.0416	21.90	0.9728	0.3677	10.88	0.6769
3DGS [22]	0.1133	18.42	0.8736	0.0330	27.54	0.9809	0.1051	20.40	0.8858
DietNeRF [18]	0.0863	22.39	0.9085	0.0274	20.89	0.9760	0.0951	22.80	0.9012
RegNeRF [36]	0.2736	9.34	0.7736	0.0300	20.88	0.9794	0.3180	10.00	0.7726
FreeNeRF [72]	0.0904	22.09	0.9083	0.0300	20.89	0.9760	0.0847	23.78	0.9153
SparseNeRF [60]	0.2530	9.45	0.7695	0.0395	20.82	0.9738	0.2997	10.01	0.7516
ZeroRF [49]	0.1038	20.86	0.8992	0.0190	31.77	0.9829	0.1264	19.80	0.8813
FSGS [81]	0.1100	19.69	0.8902	0.0274	25.48	0.9778	0.0932	22.86	0.9112
GaussianObject	0.0499	23.53	0.9313	0.0104	31.97	0.9864	0.0487	25.50	0.9358

Table 7. Comparisons of per-scene metrics of MipNeRF360 with 9 input views.

Method	bonsai			garden			kitchen		
	LPIPS ↓	PSNR ↑	SSIM ↑	LPIPS ↓	PSNR ↑	SSIM ↑	LPIPS ↓	PSNR ↑	SSIM ↑
DVGO [58]	0.3658	11.17	0.6938	0.0367	22.09	0.9747	0.3672	10.95	0.6843
3DGS [22]	0.0932	20.68	0.9004	0.0222	29.46	0.9839	0.0771	22.74	0.9149
DietNeRF [18]	0.0706	24.45	0.9263	0.0274	20.89	0.9760	0.0774	25.30	0.9247
RegNeRF [36]	0.2875	9.45	0.7706	0.0300	20.89	0.9794	0.2735	10.70	0.8050
FreeNeRF [72]	0.0788	23.99	0.9263	0.0164	33.05	0.9859	0.0702	25.96	0.9335
SparseNeRF [60]	0.2857	9.38	0.7447	0.0298	23.04	0.9776	0.3313	10.67	0.7481
ZeroRF [49]	0.0657	24.72	0.9312	0.0174	32.75	0.9841	0.0770	25.88	0.9227
FSGS [81]	0.0816	22.72	0.9164	0.0198	29.28	0.9815	0.0804	23.91	0.9213
GaussianObject	0.0382	25.65	0.9502	0.0089	33.09	0.9886	0.0353	27.11	0.9526

Table 8. Comparisons of per-scene metrics of OmniObject3D with 4 input views.

Method	backpack_016			box_043			broccoli_003		
	LPIPS ↓	PSNR ↑	SSIM ↑	LPIPS ↓	PSNR ↑	SSIM ↑	LPIPS ↓	PSNR ↑	SSIM ↑
DVGO [58]	0.2674	11.41	0.7794	0.0814	20.21	0.9455	0.0953	16.14	0.9229
3DGS [22]	0.1542	15.13	0.8505	0.0536	18.57	0.9665	0.0677	15.68	0.9458
DietNeRF [18]	0.2903	11.30	0.8183	0.1866	15.54	0.8867	0.1028	14.65	0.9172
RegNeRF [36]	0.2987	9.56	0.8022	0.1298	16.40	0.9455	0.1109	14.08	0.9239
FreeNeRF [72]	0.1358	11.57	0.8899	0.0775	17.59	0.9516	0.0570	16.36	0.9559
SparseNeRF [60]	0.2570	9.78	0.7985	0.0960	16.52	0.9437	0.1068	14.18	0.9208
ZeroRF [49]	0.0528	25.13	0.9459	0.0211	33.94	0.9827	0.0228	30.32	0.9745
FSGS [81]	0.1257	19.48	0.9089	0.0835	23.70	0.9590	0.0399	23.25	0.9670
GaussianObject	0.0425	25.61	0.9511	0.0140	33.22	0.9833	0.0138	30.59	0.9781

Method	corn_007			dinosaur_006			flower_pot_007		
	LPIPS ↓	PSNR ↑	SSIM ↑	LPIPS ↓	PSNR ↑	SSIM ↑	LPIPS ↓	PSNR ↑	SSIM ↑
DVGO [58]	0.1135	21.81	0.9279	0.1924	16.08	0.8539	0.1281	15.04	0.8951
3DGS [22]	0.0826	18.91	0.9496	0.1124	18.31	0.8952	0.0741	14.79	0.9330
DietNeRF [18]	0.0244	33.80	0.9729	0.1168	16.07	0.9161	0.0482	16.22	0.9539
RegNeRF [36]	0.1869	16.65	0.9200	0.2371	14.60	0.8838	0.1499	13.35	0.9065
FreeNeRF [72]	0.0732	24.35	0.9517	0.1071	16.01	0.9197	0.0962	15.45	0.9259
SparseNeRF [60]	0.1678	16.77	0.9041	0.1781	15.22	0.8881	0.1379	14.20	0.9139
ZeroRF [49]	0.0343	33.68	0.9694	0.0460	26.59	0.9545	0.0235	30.77	0.9759
FSGS [81]	0.0650	26.37	0.9577	0.0969	21.19	0.9266	0.0363	26.88	0.9659
GaussianObject	0.0166	34.44	0.9781	0.0349	27.68	0.9607	0.0156	31.22	0.9795

Method	gloves_009			guitar_002			hamburger_012		
	LPIPS ↓	PSNR ↑	SSIM ↑	LPIPS ↓	PSNR ↑	SSIM ↑	LPIPS ↓	PSNR ↑	SSIM ↑
DVGO [58]	0.2285	12.45	0.8229	0.1178	15.46	0.9102	0.1510	19.00	0.9028
3DGS [22]	0.1303	13.04	0.8945	0.1130	12.74	0.8995	0.0954	16.24	0.9274
DietNeRF [18]	0.1222	14.08	0.9140	0.0917	24.20	0.9342	0.2062	15.46	0.8675
RegNeRF [36]	0.1590	12.90	0.8989	0.1874	12.52	0.8660	0.1654	15.60	0.9154
FreeNeRF [72]	0.1458	13.50	0.8951	0.1004	13.44	0.9206	0.0790	17.33	0.9442
SparseNeRF [60]	0.1440	13.03	0.8912	0.3535	10.53	0.7153	0.1716	15.68	0.8914
ZeroRF [49]	0.1578	14.61	0.8793	0.0785	20.87	0.9373	0.0355	29.33	0.9634
FSGS [81]	0.1427	16.80	0.9140	0.0416	27.92	0.9659	0.0747	22.20	0.9474
GaussianObject	0.0297	26.94	0.9695	0.0141	32.37	0.9816	0.0224	31.46	0.9694

Table 9. Comparisons of per-scene metrics of OmniObject3D with 4 input views. *continued*

Method	picnic_basket_009			pineapple_013			sandwich_003			suitcase_006		
	LPIPS ↓	PSNR ↑	SSIM ↑	LPIPS ↓	PSNR ↑	SSIM ↑	LPIPS ↓	PSNR ↑	SSIM ↑	LPIPS ↓	PSNR ↑	SSIM ↑
DVGO [58]	0.1540	16.08	0.8887	0.1677	14.39	0.8747	0.0423	25.15	0.9787	0.1865	14.52	0.8697
3DGS [22]	0.0837	19.60	0.9167	0.0573	16.74	0.9484	0.0285	22.44	0.9850	0.1028	15.18	0.9331
DietNeRF [18]	0.1512	15.02	0.8940	0.0933	16.48	0.9336	0.0253	22.52	0.9851	0.0542	26.60	0.9639
RegNeRF [36]	0.1313	14.73	0.9303	0.1431	14.01	0.9005	0.0293	22.52	0.9875	0.2636	12.03	0.8587
FreeNeRF [72]	0.0772	15.82	0.9433	0.0638	16.74	0.9471	0.0293	22.52	0.9850	0.0755	25.66	0.9422
SparseNeRF [60]	0.3376	14.99	0.8717	0.1918	16.01	0.9113	0.0478	20.47	0.9750	0.2487	12.55	0.8384
ZeroRF [49]	0.0391	28.33	0.9648	0.0569	22.81	0.9413	0.0171	30.44	0.9886	0.0520	23.83	0.9611
FSGS [81]	0.0417	25.60	0.9612	0.0608	20.87	0.9447	0.0110	33.34	0.9900	0.0682	23.70	0.9528
GaussianObject	0.0220	31.44	0.9733	0.0208	28.16	0.9676	0.0072	34.34	0.9919	0.0259	28.69	0.9758

Method	timer_010			toy_plane_005			toy_truck_037			vase_012		
	LPIPS ↓	PSNR ↑	SSIM ↑	LPIPS ↓	PSNR ↑	SSIM ↑	LPIPS ↓	PSNR ↑	SSIM ↑	LPIPS ↓	PSNR ↑	SSIM ↑
DVGO [58]	0.1104	18.90	0.9345	0.0929	22.37	0.9423	0.1415	16.34	0.9075	0.1912	16.01	0.8612
3DGS [22]	0.0940	17.41	0.9407	0.0470	22.94	0.9672	0.0567	18.26	0.9583	0.1086	17.96	0.8968
DietNeRF [18]	0.1411	17.30	0.9143	0.0321	24.12	0.9752	0.1059	17.73	0.9382	0.1856	14.41	0.8637
RegNeRF [36]	0.1557	16.79	0.9310	0.0354	24.12	0.9810	0.1531	15.37	0.9240	0.3109	13.18	0.8799
FreeNeRF [72]	0.0616	18.80	0.9664	0.0354	24.12	0.9752	0.0612	18.28	0.9562	0.1309	14.74	0.9130
SparseNeRF [60]	0.1742	17.37	0.9317	0.0655	22.32	0.9603	0.1257	15.55	0.9161	0.1664	13.63	0.8939
ZeroRF [49]	0.0258	32.97	0.9848	0.0228	30.52	0.9827	0.0251	30.68	0.9758	0.0440	27.51	0.9634
FSGS [81]	0.0362	29.15	0.9782	0.0256	29.93	0.9798	0.0517	26.15	0.9588	0.0607	23.53	0.9490
GaussianObject	0.0152	33.43	0.9867	0.0102	34.30	0.9884	0.0137	32.23	0.9820	0.0327	29.10	0.9676

Table 10. Comparisons of per-scene metrics of OmniObject3D with 6 input views.

Method	backpack_016			box_043			broccoli_003		
	LPIPS ↓	PSNR ↑	SSIM ↑	LPIPS ↓	PSNR ↑	SSIM ↑	LPIPS ↓	PSNR ↑	SSIM ↑
DVGO [58]	0.2363	12.56	0.8040	0.1028	19.74	0.9412	0.0853	18.16	0.9385
3DGS [22]	0.0901	21.26	0.9122	0.0582	18.16	0.9607	0.0483	16.77	0.9621
DietNeRF [18]	0.2117	11.25	0.8546	0.1111	17.25	0.9325	0.0994	15.03	0.9267
RegNeRF [36]	0.2818	10.08	0.8291	0.1251	15.85	0.9420	0.0483	16.84	0.9663
FreeNeRF [72]	0.2255	12.30	0.8181	0.0530	18.68	0.9656	0.0483	16.84	0.9625
SparseNeRF [60]	0.4828	11.35	0.7691	0.1030	18.16	0.9602	0.0483	16.84	0.9625
ZeroRF [49]	0.0494	27.87	0.9529	0.0195	36.07	0.9843	0.0212	32.54	0.9768
FSGS [81]	0.0815	22.34	0.9308	0.0266	32.41	0.9799	0.1163	20.96	0.9473
GaussianObject	0.0318	27.60	0.9593	0.0121	35.15	0.9868	0.0108	32.78	0.9842

Method	corn_007			dinosaur_006			flower_pot_007		
	LPIPS ↓	PSNR ↑	SSIM ↑	LPIPS ↓	PSNR ↑	SSIM ↑	LPIPS ↓	PSNR ↑	SSIM ↑
DVGO [58]	0.1056	22.43	0.9540	0.1456	17.91	0.8879	0.1348	15.36	0.8890
3DGS [22]	0.0796	19.22	0.9551	0.1030	19.04	0.8968	0.0675	15.43	0.9392
DietNeRF [18]	0.0225	35.23	0.9775	0.1905	14.69	0.8592	0.0482	16.22	0.9539
RegNeRF [36]	0.1444	17.56	0.9413	0.2226	14.38	0.8905	0.1323	13.50	0.9122
FreeNeRF [72]	0.0794	19.44	0.9523	0.0970	16.26	0.9275	0.0525	16.22	0.9539
SparseNeRF [60]	0.0793	19.42	0.9523	0.3566	15.12	0.8636	0.1861	12.72	0.8600
ZeroRF [49]	0.0309	34.98	0.9726	0.0409	29.03	0.9633	0.0217	32.83	0.9791
FSGS [81]	0.0511	29.35	0.9634	0.0503	26.38	0.9577	0.0386	27.17	0.9658
GaussianObject	0.0135	35.77	0.9821	0.0256	29.65	0.9708	0.0107	34.40	0.9866

Method	gloves_009			guitar_002			hamburger_012		
	LPIPS ↓	PSNR ↑	SSIM ↑	LPIPS ↓	PSNR ↑	SSIM ↑	LPIPS ↓	PSNR ↑	SSIM ↑
DVGO [58]	0.1373	15.00	0.9011	0.0803	17.61	0.9368	0.1697	18.75	0.9068
3DGS [22]	0.1284	13.42	0.8967	0.1176	12.50	0.8944	0.0949	16.48	0.9278
DietNeRF [18]	0.1647	13.92	0.8797	0.0401	28.63	0.9650	0.1563	16.14	0.9029
RegNeRF [36]	0.1919	13.12	0.8849	0.1228	14.95	0.9105	0.2122	14.52	0.9015
FreeNeRF [72]	0.0905	14.39	0.9331	0.0272	33.19	0.9767	0.0790	17.33	0.9442
SparseNeRF [60]	0.1672	13.14	0.8744	0.3992	10.46	0.7581	0.5058	13.82	0.8368
ZeroRF [49]	0.0352	30.52	0.9728	0.0669	23.41	0.9423	0.0292	33.60	0.9710
FSGS [81]	0.0930	20.34	0.9333	0.0509	26.17	0.9627	0.0512	27.72	0.9568
GaussianObject	0.0214	30.75	0.9788	0.0116	34.24	0.9861	0.0152	34.29	0.9801

Table 11. Comparisons of per-scene metrics of OmniObject3D with 6 input views. *continued*

Method	picnic_basket_009			pineapple_013			sandwich_003			suitcase_006		
	LPIPS ↓	PSNR ↑	SSIM ↑	LPIPS ↓	PSNR ↑	SSIM ↑	LPIPS ↓	PSNR ↑	SSIM ↑	LPIPS ↓	PSNR ↑	SSIM ↑
DVGO [58]	0.1371	17.15	0.9021	0.1448	17.23	0.8945	0.0793	25.23	0.9663	0.1489	15.70	0.9050
3DGS [22]	0.0490	26.20	0.9494	0.0682	16.16	0.9388	0.0374	21.32	0.9784	0.1026	15.19	0.9331
DietNeRF [18]	0.1264	15.24	0.9123	0.0564	16.74	0.9472	0.0253	22.52	0.9851	0.0373	29.00	0.9750
RegNeRF [36]	0.0772	15.82	0.9524	0.1467	14.15	0.8969	0.0293	22.52	0.9875	0.1351	15.80	0.9186
FreeNeRF [72]	0.0772	15.82	0.9433	0.0638	16.74	0.9471	0.0293	22.52	0.9850	0.0682	26.99	0.9469
SparseNeRF [60]	0.3520	15.91	0.9024	0.1997	15.63	0.9061	0.0591	20.90	0.9734	0.2311	15.50	0.8714
ZeroRF [49]	0.0337	31.11	0.9698	0.0257	29.64	0.9671	0.0058	38.85	0.9958	0.0513	26.33	0.9676
FSGS [81]	0.0283	31.43	0.9742	0.0299	28.42	0.9697	0.0079	37.49	0.9938	0.1395	18.73	0.9197
GaussianObject	0.0185	33.30	0.9779	0.0146	31.03	0.9797	0.0041	38.29	0.9954	0.0192	30.54	0.9826

Method	timer_010			toy_plane_005			toy_truck_037			vase_012		
	LPIPS ↓	PSNR ↑	SSIM ↑	LPIPS ↓	PSNR ↑	SSIM ↑	LPIPS ↓	PSNR ↑	SSIM ↑	LPIPS ↓	PSNR ↑	SSIM ↑
DVGO [58]	0.1335	19.63	0.9395	0.0919	21.98	0.9451	0.1244	18.42	0.9176	0.1343	18.49	0.9125
3DGS [22]	0.0751	18.15	0.9556	0.0559	22.24	0.9639	0.0583	18.23	0.9581	0.0822	21.16	0.9204
DietNeRF [18]	0.1221	16.94	0.9225	0.0321	24.12	0.9752	0.0988	17.53	0.9335	0.2242	13.73	0.8517
RegNeRF [36]	0.1444	16.39	0.9410	0.0354	24.12	0.9810	0.1553	15.88	0.9187	0.2404	13.07	0.8783
FreeNeRF [72]	0.0616	18.80	0.9664	0.0354	24.12	0.9752	0.0612	18.28	0.9562	0.0952	15.51	0.9354
SparseNeRF [60]	0.1266	17.09	0.9349	0.0569	23.93	0.9688	0.1290	15.97	0.9122	0.2075	13.66	0.8827
ZeroRF [49]	0.0246	34.57	0.9860	0.0128	36.87	0.9896	0.0218	33.79	0.9801	0.0377	31.05	0.9716
FSGS [81]	0.0582	25.42	0.9655	0.0207	31.97	0.9838	0.1065	19.30	0.9370	0.0782	22.55	0.9478
GaussianObject	0.0139	34.73	0.9885	0.0075	36.59	0.9918	0.0080	35.40	0.9885	0.0253	31.69	0.9763

Table 12. Comparisons of per-scene metrics of OmniObject3D with 9 input views.

Method	backpack_016			box_043			broccoli_003		
	LPIPS ↓	PSNR ↑	SSIM ↑	LPIPS ↓	PSNR ↑	SSIM ↑	LPIPS ↓	PSNR ↑	SSIM ↑
DVGO [58]	0.2299	12.43	0.8179	0.0664	22.20	0.9677	0.0683	21.03	0.9618
3DGS [22]	0.0519	26.80	0.9494	0.0506	18.65	0.9669	0.0531	16.45	0.9552
DietNeRF [18]	0.1806	11.48	0.8684	0.0481	18.68	0.9656	0.0995	14.19	0.9211
RegNeRF [36]	0.2967	10.46	0.8276	0.1051	17.39	0.9490	0.0483	16.84	0.9663
FreeNeRF [72]	0.2422	12.39	0.8084	0.0530	18.68	0.9656	0.0483	16.84	0.9625
SparseNeRF [60]	0.4932	10.46	0.7481	0.0615	18.59	0.9639	0.2476	13.34	0.8900
ZeroRF [49]	0.0459	30.15	0.9582	0.0184	37.80	0.9857	0.0216	33.42	0.9775
FSGS [81]	0.1250	14.84	0.8963	0.0226	33.72	0.9858	0.0169	33.03	0.9817
GaussianObject	0.0229	31.41	0.9737	0.0089	37.98	0.9910	0.0085	34.91	0.9882

Method	corn_007			dinosaur_006			flower_pot_007		
	LPIPS ↓	PSNR ↑	SSIM ↑	LPIPS ↓	PSNR ↑	SSIM ↑	LPIPS ↓	PSNR ↑	SSIM ↑
DVGO [58]	0.0921	22.05	0.9598	0.0985	19.56	0.9269	0.0987	19.15	0.9319
3DGS [22]	0.0801	19.11	0.9510	0.0620	23.57	0.9377	0.0622	15.65	0.9438
DietNeRF [18]	0.0184	36.58	0.9824	0.2514	14.57	0.8359	0.0482	16.22	0.9539
RegNeRF [36]	0.0870	20.45	0.9546	0.1914	14.51	0.8951	0.0525	16.22	0.9598
FreeNeRF [72]	0.0221	36.42	0.9779	0.0970	16.26	0.9275	0.0525	16.22	0.9539
SparseNeRF [60]	0.2863	18.94	0.9340	0.4706	13.86	0.8191	0.1816	13.70	0.8855
ZeroRF [49]	0.0352	35.69	0.9715	0.0393	30.28	0.9679	0.0199	34.60	0.9816
FSGS [81]	0.0280	34.01	0.9792	0.0533	27.19	0.9593	0.0295	30.55	0.9750
GaussianObject	0.0089	38.33	0.9879	0.0201	31.61	0.9780	0.0087	36.13	0.9896

Method	gloves_009			guitar_002			hamburger_012		
	LPIPS ↓	PSNR ↑	SSIM ↑	LPIPS ↓	PSNR ↑	SSIM ↑	LPIPS ↓	PSNR ↑	SSIM ↑
DVGO [58]	0.0879	17.36	0.9425	0.0481	21.24	0.9614	0.0896	23.11	0.9592
3DGS [22]	0.1239	13.78	0.9039	0.1060	12.90	0.9060	0.0937	16.56	0.9282
DietNeRF [18]	0.1353	13.77	0.8923	0.0318	32.15	0.9730	0.1504	16.01	0.9007
RegNeRF [36]	0.0905	14.39	0.9428	0.0928	16.97	0.9268	0.0790	17.33	0.9567
FreeNeRF [72]	0.1393	13.64	0.8944	0.0236	35.56	0.9818	0.0790	17.33	0.9442
SparseNeRF [60]	0.1584	13.29	0.8768	0.2553	19.14	0.8907	0.4415	15.47	0.8795
ZeroRF [49]	0.0349	31.94	0.9753	0.0768	20.01	0.9370	0.0314	34.14	0.9713
FSGS [81]	0.0817	21.46	0.9422	0.0436	28.66	0.9693	0.0259	33.34	0.9781
GaussianObject	0.0180	32.89	0.9838	0.0100	35.55	0.9888	0.0103	37.09	0.9875

Table 13. Comparisons of per-scene metrics of OmniObject3D with 9 input views. *continued*

Method	picnic_basket_009			pineapple_013			sandwich_003			suitcase_006		
	LPIPS ↓	PSNR ↑	SSIM ↑	LPIPS ↓	PSNR ↑	SSIM ↑	LPIPS ↓	PSNR ↑	SSIM ↑	LPIPS ↓	PSNR ↑	SSIM ↑
DVGO [58]	0.1501	16.50	0.9012	0.0927	18.63	0.9393	0.0509	25.44	0.9818	0.0965	17.72	0.9430
3DGS [22]	0.0232	32.98	0.9768	0.0573	16.73	0.9483	0.0316	21.91	0.9825	0.1026	15.19	0.9331
DietNeRF [18]	0.1416	13.74	0.8889	0.1247	14.14	0.8914	0.0253	22.52	0.9851	0.0325	30.99	0.9799
RegNeRF [36]	0.1746	13.91	0.8965	0.0638	16.74	0.9534	0.0293	22.52	0.9875	0.0317	32.63	0.9903
FreeNeRF [72]	0.0772	15.82	0.9433	0.0638	16.74	0.9471	0.0293	22.52	0.9850	0.0510	30.81	0.9699
SparseNeRF [60]	0.4269	14.14	0.8208	0.4313	14.55	0.8322	0.0448	22.50	0.9843	0.0438	31.75	0.9803
ZeroRF [49]	0.0320	33.12	0.9735	0.0254	30.79	0.9692	0.0057	39.80	0.9961	0.0463	28.34	0.9722
FSGS [81]	0.0393	28.61	0.9712	0.0186	31.83	0.9807	0.0076	35.88	0.9945	0.0452	29.53	0.9746
GaussianObject	0.0139	35.27	0.9836	0.0109	33.00	0.9858	0.0029	41.15	0.9971	0.0143	32.99	0.9876
Method	timer_010			toy_plane_005			toy_truck_037			vase_012		
	LPIPS ↓	PSNR ↑	SSIM ↑	LPIPS ↓	PSNR ↑	SSIM ↑	LPIPS ↓	PSNR ↑	SSIM ↑	LPIPS ↓	PSNR ↑	SSIM ↑
DVGO [58]	0.1811	17.27	0.9222	0.2574	16.89	0.8464	0.1297	17.93	0.9270	0.1154	18.89	0.9242
3DGS [22]	0.0450	28.44	0.9669	0.0499	22.88	0.9650	0.0557	18.27	0.9584	0.0566	24.65	0.9486
DietNeRF [18]	0.1010	17.56	0.9359	0.0321	24.12	0.9752	0.1074	17.25	0.9337	0.2255	13.52	0.8559
RegNeRF [36]	0.0616	18.80	0.9725	0.0354	24.12	0.9810	0.0612	18.28	0.9647	0.2283	13.26	0.8901
FreeNeRF [72]	0.0616	18.80	0.9664	0.0354	24.12	0.9752	0.0612	18.28	0.9562	0.0952	15.51	0.9354
SparseNeRF [60]	0.1180	17.47	0.9353	0.0354	24.10	0.9752	0.1425	15.93	0.9067	0.2013	14.46	0.8883
ZeroRF [49]	0.0231	35.46	0.9877	0.0124	37.76	0.9902	0.0215	34.09	0.9805	0.0366	32.43	0.9742
FSGS [81]	0.0427	28.50	0.9804	0.0204	32.56	0.9829	0.0686	23.09	0.9565	0.0406	28.96	0.9732
GaussianObject	0.0106	36.87	0.9921	0.0058	38.48	0.9941	0.0072	36.72	0.9905	0.0219	32.94	0.9799

Table 14. Comparisons of per-scene metrics of OpenIllumination with 4 input views. Methods with †means the metrics are from the ZeroRF paper [49].

Method	stone			pumpkin			toy			potato		
	LPIPS ↓	PSNR ↑	SSIM ↑	LPIPS ↓	PSNR ↑	SSIM ↑	LPIPS ↓	PSNR ↑	SSIM ↑	LPIPS ↓	PSNR ↑	SSIM ↑
DVGO [58]	0.0829	21.99	0.8957	0.0945	23.07	0.9370	0.0928	21.69	0.9121	0.1196	21.37	0.9097
3DGS [22]	0.2890	10.93	0.8107	0.2950	11.43	0.8692	0.2898	11.16	0.8213	0.3063	12.03	0.8639
DietNeRF† [18]	0.0850	24.05	0.9210	0.0600	26.54	0.9700	0.0790	24.98	0.9490	0.1030	23.00	0.9490
RegNeRF† [36]	0.4830	10.26	0.6020	0.4650	11.74	0.7490	0.4760	10.04	0.6370	0.5050	11.63	0.7190
FreeNeRF† [72]	0.2100	12.91	0.7790	0.3120	11.54	0.8270	0.3510	10.79	0.7860	0.4610	11.70	0.7960
SparseNeRF [60]	0.2600	12.99	0.8315	0.3029	11.44	0.7991	0.1181	13.67	0.9200	0.2821	13.26	0.8798
ZeroRF† [49]	0.0720	25.07	0.9180	0.0750	26.07	0.9610	0.0890	23.72	0.9360	0.0960	26.27	0.9460
GaussianObject	0.0542	23.96	0.9204	0.0538	25.89	0.9579	0.0493	24.95	0.9453	0.0690	25.09	0.9424
Method	pine			shroom			cow			cake		
	LPIPS ↓	PSNR ↑	SSIM ↑	LPIPS ↓	PSNR ↑	SSIM ↑	LPIPS ↓	PSNR ↑	SSIM ↑	LPIPS ↓	PSNR ↑	SSIM ↑
DVGO [58]	0.1177	19.04	0.8791	0.1754	18.13	0.8533	0.1854	18.14	0.8523	0.0790	25.74	0.9396
3DGS [22]	0.3038	10.07	0.8095	0.3594	11.03	0.8182	0.3157	11.81	0.8573	0.2475	13.54	0.9133
DietNeRF† [18]	0.0930	20.94	0.9240	0.1660	19.91	0.9110	0.2070	16.30	0.8940	0.0600	28.97	0.9710
RegNeRF† [36]	0.4860	9.37	0.5710	0.5510	10.66	0.6580	0.4600	11.99	0.7480	0.3590	17.21	0.8680
FreeNeRF† [72]	0.2200	10.17	0.7910	0.5540	11.46	0.7510	0.4580	11.18	0.7460	0.2990	17.95	0.8990
SparseNeRF [60]	0.1412	12.28	0.8981	0.2026	13.33	0.8963	0.2170	13.64	0.9003	0.2584	18.21	0.9214
ZeroRF† [49]	0.1160	20.68	0.9030	0.1340	23.14	0.9120	0.1390	21.91	0.9050	0.0580	29.44	0.9650
GaussianObject	0.0761	21.68	0.9143	0.0872	24.16	0.9211	0.0970	22.81	0.9208	0.0499	28.58	0.9613

Table 15. Comparisons of per-scene metrics of OpenIllumination with 6 input views. Methods with †means the metrics are from the ZeroRF paper [49].

Method	stone			pumpkin			toy			potato		
	LPIPS ↓	PSNR ↑	SSIM ↑	LPIPS ↓	PSNR ↑	SSIM ↑	LPIPS ↓	PSNR ↑	SSIM ↑	LPIPS ↓	PSNR ↑	SSIM ↑
DVGO [58]	0.0621	24.22	0.9132	0.0682	25.82	0.9527	0.0675	24.44	0.9313	0.0931	24.24	0.9279
3DGS [22]	0.3139	10.87	0.7702	0.2547	12.98	0.8823	0.2993	11.10	0.7943	0.3197	11.70	0.8462
DietNeRF† [18]	0.0850	24.87	0.9210	0.0730	24.80	0.9660	0.0860	25.37	0.9440	0.0870	25.63	0.9550
RegNeRF† [36]	0.2880	13.80	0.8480	0.3500	13.58	0.8480	0.2370	13.54	0.8840	0.3480	13.92	0.8540
FreeNeRF† [72]	0.2360	11.62	0.7910	0.2930	11.71	0.8640	0.3460	10.65	0.8140	0.3970	11.35	0.8320
SparseNeRF [60]	0.2452	12.91	0.8091	0.1468	14.81	0.9406	0.1181	13.67	0.9200	0.3519	12.36	0.8614
ZeroRF† [49]	0.0630	26.30	0.9290	0.0640	27.87	0.9660	0.0620	27.28	0.9500	0.0840	27.26	0.9510
GaussianObject	0.0430	26.07	0.9301	0.0415	28.06	0.9648	0.0402	27.55	0.9535	0.0571	26.56	0.9495

Method	pine			shroom			cow			cake		
	LPIPS ↓	PSNR ↑	SSIM ↑	LPIPS ↓	PSNR ↑	SSIM ↑	LPIPS ↓	PSNR ↑	SSIM ↑	LPIPS ↓	PSNR ↑	SSIM ↑
DVGO [58]	0.0924	20.61	0.8976	0.1327	20.88	0.8891	0.1331	22.00	0.8997	0.0571	28.15	0.9562
3DGS [22]	0.2687	11.73	0.8112	0.3633	11.49	0.7671	0.3246	11.55	0.8329	0.2277	14.38	0.9174
DietNeRF† [18]	0.1190	18.16	0.9020	0.1190	23.71	0.9300	0.1330	21.50	0.9300	0.0590	29.58	0.9730
RegNeRF† [36]	0.3370	11.87	0.8070	0.3290	13.22	0.8630	0.4050	13.07	0.8070	0.1280	19.66	0.9580
FreeNeRF† [72]	0.3280	8.85	0.7530	0.5050	10.12	0.7640	0.4420	11.09	0.7840	0.2650	16.33	0.9000
SparseNeRF [60]	0.3807	6.61	0.5537	0.3551	11.92	0.8290	0.2227	13.64	0.8983	0.2840	16.46	0.9100
ZeroRF† [49]	0.0880	22.26	0.9180	0.1060	26.34	0.9280	0.1180	23.74	0.9210	0.0520	31.00	0.9690
GaussianObject	0.0629	23.25	0.9264	0.0712	26.35	0.9307	0.0804	24.43	0.9325	0.0389	30.06	0.9673